

Optimization of Orally Bioavailable Enhancer of Zeste Homolog 2 (EZH2) Inhibitors Using Ligand and Property-Based Design Strategies: Identification of Development Candidate (*R*)-5,8-Dichloro-7-(methoxy(oxetan-3-yl)methyl)-2-((4-methoxy-6-methyl-2-oxo-1,2-dihydropyridin-3-yl)methyl)-3,4-dihydroisoquinolin-1(2*H*)-one (PF-06821497)

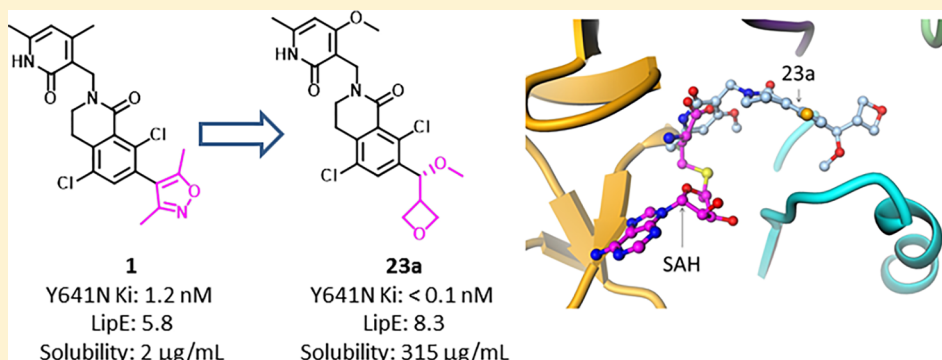
Pei-Pei Kung,^{*,†,‡} Patrick Bingham,[‡] Alexei Brooun,[†] Michael Collins,[†] Ya-Li Deng,[†] Dac Dinh,[‡] Connie Fan,[†] Ketan S. Gajiwala,[†] Rita Grantner,[‡] Hovhannes J. Gukasyan,^{||} Wenyue Hu,[†] Buwen Huang,[†] Robert Kania,[†] Susan E. Kephart,[†] Cody Krivacic,[‡] Robert A. Kumpf,[†] Penney Khamphavong,^{||} Manfred Kraus,[‡] Wei Liu,[†] Karen A. Maegley,[‡] Lisa Nguyen,[‡] Shijian Ren,[▽] Dan Richter,[†] Robert A. Rollins,^{‡,§} Neal Sach,[†] Shikhar Sharma,[‡] John Sherrill,[‡] Jillian Spangler,[†] Albert E. Stewart,[†] Scott Sutton,[†] Sean Uryu,[‡] Dominique Verhelle,[‡] Hui Wang,[‡] Shuiwang Wang,[▽] Martin Wythes,[†] Shuibo Xin,[▽] Shinji Yamazaki,[§] Huichun Zhu,[†] JinJiang Zhu,[†] Luke Zehnder,[†] and Martin Edwards[†]

[†]Oncology Medicinal Chemistry, [‡]Oncology Research Unit, [§]Pharmacokinetics, Dynamics, and Metabolism, ^{||}Pharmaceutical Science Research Enabling Group, and [▽]Drug Safety Research and Development, Pfizer Global Research and Development, La Jolla Laboratories, 10770 Science Center Drive, San Diego, California 92121, United States

[#]Pfizer Global Research and Development, 401 N. Middletown Road, Pearl River, New York 10965, United States

[▽]WuXi AppTec, 288 Fute Zhong Road, Waigaoqiao Free Trade Zone, Shanghai 200131, China

Supporting Information



ABSTRACT: A new series of lactam-derived EZH2 inhibitors was designed via ligand-based and physicochemical-property-based strategies to address metabolic stability and thermodynamic solubility issues associated with previous lead compound 1. The new inhibitors incorporated an sp³ hybridized carbon atom at the 7-position of the lactam moiety present in lead compound 1 as a replacement for a dimethylisoxazole group. This transformation enabled optimization of the physicochemical properties and potency compared to compound 1. Analysis of relationships between calculated log D (clogD) values and in vitro metabolic stability and permeability parameters identified a clogD range that afforded an increased probability of achieving favorable ADME data in a single molecule. Compound 23a exhibited the best overlap of potency and pharmaceutical properties as well as robust tumor growth inhibition in vivo and was therefore advanced as a development candidate (PF-06821497). A crystal structure of 23a in complex with the three-protein PRC2 complex enabled understanding of the key structural features required for optimal binding.

INTRODUCTION

Polycomb group (PcG) and trithorax group (TrxG) proteins are key regulators of heritable gene expression patterns.^{1,2} PcG proteins are present in two major evolutionarily conserved

Received: September 27, 2017

Published: December 6, 2017

multiprotein complexes, known as polycomb repressive complexes 1 and 2 (PRC1 and PRC2). The PRC2 complex contains three core subunits: (1) EZH2 (enhancer of zeste homolog 2) or its closely related homolog EZH1, (2) SUZ12 (suppressor of zeste 12), and (3) EED (embryonic ectoderm development) along with additional subcomponents such as histone and DNA interacting proteins RbAp46/48 and AEBP2.^{3,4} The EZH2 histone methyltransferase subunit of the complex contains the catalytic SET (Su[var]3-9, enhancer of zeste, trithorax) domain which catalyzes the mono-, di-, and trimethylation of lysine 27 on histone H3 (H3K27me, me2, and me3).

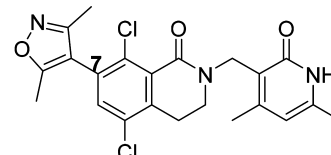
Epigenetic alterations are a recognized hallmark of cancer cells, and several lines of evidence link aberrant EZH2 activity to tumor initiation and progression. EZH2 is overexpressed in multiple solid tumors and hematological malignancies, and elevated expression is often correlated with disease progression and poor survival.⁵ In addition, oncogenic activating point mutations in the SET domain of EZH2 have been identified in diffuse large B-cell lymphoma (DLBCL) and follicular lymphoma (FL).^{6–10} These genetic alterations in EZH2 alter the substrate specificity of the enzyme, resulting in elevated H3K27me3 levels and enhanced transcriptional repression. Moreover, cell lines harboring these mutations display sensitivity to small molecule EZH2 inhibitors, supporting the importance of EZH2 catalytic activity in these cancers. In addition to the genetic alterations of EZH2 in hematological cancers, cancer specific dependencies have also been identified in solid tumors in the context of wild-type EZH2. Genetic and pharmacological inhibition of EZH2 has uncovered synthetic lethal relationships in lung, ovarian, malignant rhabdoid, and synovial sarcoma models harboring mutations in the SMARCA2, SMARCA4, ARID1A, and SNF5/INI-1/SMARCB1 components of the SWI/SNF chromatin remodeling complex.^{11–16} More recently, it has been demonstrated that EZH2 activity regulates transcriptional programs that control differentiation status and drug resistance in small-cell lung cancer and neuroendocrine prostate cancer.^{17–19} Collectively, these data provide a compelling rationale for the inhibition of EZH2 enzymatic function as a potential therapeutic approach for the treatment of cancer.

The abundance of preclinical data supporting EZH2 as a therapeutic target has stimulated drug discovery programs aimed at developing small molecule inhibitors that block EZH2 enzymatic function. Several examples of such inhibitors including GSK-126,¹⁰ tazemetostat (EPZ-6438),²⁰ and CPI-1205²¹ have entered clinical trials for the treatment of diffuse large B-cell lymphoma (DLBCL), follicular lymphoma (FL), and SNF5/INI-1/SMARCB1 genetically defined solid tumors. The reported interim phase II objective response rates (ORR) for tazemetostat in DLBCL and FL patients harboring tumors with mutant EZH2 proteins were 29% and 92%, respectively. In contrast, these phase II ORR values dropped to 15% and 26%, respectively, in DLBCL and FL patients bearing tumors containing wild type EZH2.²² These results highlighted the important role for enhanced EZH2 catalytic function in these disease settings and demonstrated great potential for EZH2 inhibitors as new therapeutic options for these DLBCL and FL patients. In contrast to targeting the enzymatic function of the PRC2 complex, binders of the EED H3K27me3 pocket were also pursued to modulate the PRC2 complex activity.^{23a,b} These efforts provided additional confidence that targeting the PRC2

complex is a viable drug discovery strategy for identifying new cancer therapies.

RESULTS AND DISCUSSION

We previously described a series of lactam-containing molecules as novel inhibitors of the EZH2 enzyme.²⁴ An optimized representative of this compound class displayed potent EZH2 inhibitory activity in enzymatic and cell-based assays along with impressive tumor growth inhibition effects in a Karpas-422 xenograft model (1, Figure 1). However,



logD: 3.1
EZH2 Y641N Ki: 1.15 nM
HLM CL: 169 μL/min/mg protein
Hep CL: 75 μL/min/million cells
MDCK-LE: 15.7 × 10⁻⁶ cm/sec
Karpas-422 cell H3K27me3 IC₅₀: 17 nM
Karpas-422 cell proliferation IC₅₀: 23 nM
Kinetic solubility: 95 μM
Crystalline form melting point: 246 °C
Thermodynamic solubility: 2 μg/mL

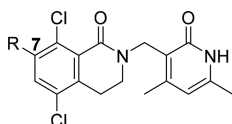
Figure 1. In vitro properties of compound 1.

compound 1 also exhibited unfavorable metabolic stability in human liver microsome (HLM)/hepatocyte clearance assays along with poor thermodynamic solubility (Figure 1). These undesirable attributes prohibited further development of the molecule, and we therefore sought to improve these ADME and physicochemical parameters in order to identify a compound that could be advanced into clinical trials. In this report, we describe our progress in optimizing the HLM clearance (target of ≤30 (μL/min)/mg protein)^{25a,b} and thermodynamic solubility properties of lactams related to compound 1 while maintaining acceptable in vitro permeability characteristics (as measured by MDCK-LE, target of ≥5 × 10⁻⁶ cm/s)²⁶ and EZH2 inhibition in both biochemical and cellular assessments.

Our optimization efforts started by replacing the dimethylisoxazole moiety present in 1 with various nonaromatic moieties that incorporated sp³ centers attached to the 7-position of the bicyclic lactam moiety. On the basis of prior literature reports, these alterations were anticipated to favorably impact the solubility properties of the new inhibitors relative to compound 1.^{27,28} Importantly, our prior studies with lactam-containing EZH2 inhibitors related to 1 indicated that the molecular region occupied by the dimethylisoxazole moiety was much more amenable to structural modification relative to other portions of the molecule. Unfortunately, we did not have supporting crystallographic data at the time we initiated these efforts to guide the new optimization efforts. Accordingly, we adopted a ligand-based dimethylisoxazole replacement strategy with an initial goal of maintaining presumed protein–ligand contacts related to the two isoxazole methyl groups that our previous studies had shown were critical for potent anti-EZH2 activity.

As shown in Table 1, a lactam-containing compound (compound 2a) bearing a 1-methoxypropyl substituent as a dimethylisoxazole replacement exhibited encouraging EZH2

Table 1. Impact of R Group on Potency, log D, and Kinetic Solubility^f



Cpd# ^a	R	Y641N biochem. K _i (nM) ^b	Karpas422 cell H3K27me3 IC ₅₀ (nM) ^c	Karpas422 cell Prolif. IC ₅₀ (nM) ^d	HLM (μL/min/mg protein)	MDCK- LE (x10 ⁻⁶ cm/sec)	logD ^e (clogD)	sol. (μM)
1		1.15	17	23	107	15.7	3.1 (3.2)	93
2a (+)		9	72	183	105	18.2	3.9 (3.5)	33
2b (-)		8	65	270	119	13.5	3.9 (3.5)	44
3a (+)		130	1045 ^e	714 ^e	18	15	3.1 (2.8)	59
3b (-)		420	5347	3551	8	15.7	3.1 (2.8)	56
4a (+)		17	129	186	15.8	12.4	2.6 (2.6)	131
4b (-)		260	1040	1502	12.4	15	2.5 (2.6)	143
5a (+)		4.6	139	124	66.3	10.9	2.8 (3.0)	324
5b (-)		14	682	502	67.6	10.9	2.9 (3.0)	443
6a (-)		0.24	10	15	21.3	2.9	2.0 (2.1)	570
6b (-)		0.38	15	17	25.9	2.5	2.1 (2.0)	508
6c Ent-6a (+)		1260	2911	3952	25.3	3.0	2.0 (2.1)	537
6d Ent-6b (+)		150	1013	1038	20	2.7	2.1 (2.0)	522
7a (ND)		10	41	57	37.6	14.6	2.4 (2.2)	400
7b (+)		8	40	63	51.6	4.1	2.1 (2.4)	430
7c Ent-7a (+)		110	1024	535	43	8.5	2.5 (2.2)	576
7d Ent-7b (-)		135	1572	1224	70.3	4.3	2.1 (2.4)	550

Cpd# ^a	R	Y641N biochem. K _i (nM) ^b	Karpas422 cell H3K27me3 IC ₅₀ (nM) ^c	Karpas422 cell Prolif. IC ₅₀ (nM) ^c	HLM (μ L/min/mg protein)	MDCK- LE ($\times 10^6$ cm/sec)	logD ^d (clogD)	sol. (μ M)
8a (-)		0.15	11	11	41.5	2.9	2.3 (2.3)	540
8b (+)		3270	14811	4404	34.7	2.9	2.3 (2.3)	496
9a (-)		34	427	282	158	26	3.3 (3.2)	55.3
9b (+)		49	1305	696	190	37.6	3.4 (3.2)	49
10a (+)		0.6	7	25	108.3	17.1	3.0 (2.9)	436
10b Ent- 10c (+)		1.9	47	50	128.2	18.7	3.0 (2.9)	439
10c (-)		30	494	406	93.3	15.4	3.0 (2.9)	457
10d Ent- 10a (-)		130	1099	175	135.7	18.4	3.0 (2.9)	414.6
11a (+)		0.10	9	19	129.3	13.3	3.4 (3.1)	57.5
11b (-)		310	1460	1153	130.3	16.5	3.5 (3.1)	57.2
12a (+)		<0.1	9	11	<10.2	2.7	1.4 (1.4)	639
12b (-)		260	1130	2320	<13.4	2.3	1.5 (1.3)	499
13a (+)		0.15	11	22	92.6	11.5	2.9 (2.6)	532
13b Ent- 13a		157	2002	1619	50.3	8.1	2.9 (2.6)	498

^aAll compounds bearing chiral centers are single stereoisomers. To help depict enantiomeric pairs, the sign of the optical rotation is provided below compound number. ^b K_i values are geometric mean values from at least three independent experiments. For each experiment, K_i values are determined from 11-point dose-response curves with each dose performed in duplicate. ^cUnless otherwise indicated, the reported IC₅₀ values are the geometric mean of values from two independent experiments. ^dThe log D was measured at pH 7.4. ^eSingle determination. ^fND: not determined.

inhibition activity in biochemical assessments employing the Y641N mutant form of the enzyme.²⁹ The 1-methoxypropyl moiety was designed based on its ability to mimic the spatial location of the two methyl groups present in the dimethylisoxazole of compound **1** (Figure 2). As expected, on the basis of its biological mechanism of action, compound **2a** inhibited EZH2-mediated increases in histone methylation as evidenced by reduced H3K27me3 levels in Karpas-422 cells. These attributes afforded relatively potent antiproliferative effects when compound **2a** was tested against Karpas-422 cells in *in vitro* assessments (Table 1). These biological activities confirmed that introduction of the sp^3 -carbon atom at the lactam 7-position was tolerated and supported the continued optimization of the new inhibitor series.

We then prepared several additional analogs related to **2a** in an effort to improve EZH2 inhibition activity and in vitro ADME properties. To help maximize lipophilic ligand efficiency (LipE)³⁰ and increase the chances of achieving good metabolic

stability, a key feature of our inhibitor design strategy was to target low $\log D$. This strategy required the inclusion of various heteroatoms (typically oxygen atoms) into the sp^3 -containing moieties that were employed as dimethylisoxazole replacements. In addition, the enantiomer of **2a** (compound **2b**) exhibited similar potencies in the described biological assessments (Table 1). As shown in Figure 2, both **2a** and **2b** could reasonably mimic the spatial orientation of the two methyl groups present in the dimethylisoxazole of compound **1** and were thus likely to maintain similar interactions with the EZH2 protein. Given the near-equivalent activities exhibited by compounds **2a** and **2b**, we purposefully synthesized the new lactam-containing compounds in racemic form (or as mixtures of diastereomers) and relied on achiral and/or chiral separation techniques to provide purified single isomers for subsequent biological assessments. For selected compounds, the absolute configurations of the sp^3 centers were determined by obtaining small molecule crystal structures. We also monitored the kinetic

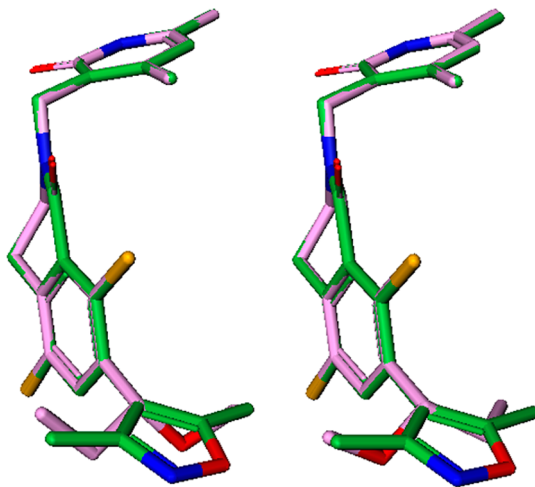


Figure 2. Overlay of minimized ligand conformations of **2a** and **2b** with compound **1**.

solubility of all newly synthesized compounds to ensure that the molecules had good potential to achieve the desired improvement on the poor thermodynamic solubility exhibited by compound **1** ($2\ \mu\text{g}/\text{mL}$ in water with 0.5% CMC and 0.1% polysorbate 80 at 25°C). Although determination of the latter parameter required distinct assessments employing crystalline forms of the test compounds, we anticipated that new molecules with poor kinetic solubility values would be unlikely to exhibit attractive thermodynamic solubility properties.

As shown in **Table 1**, removal of the methyl group from the methoxy group present in compounds **2a** and **2b** resulted in significant loss of EZH2 inhibition (compounds **3a** and **3b**). This result suggested that new moieties appended to the bicyclic lactam inhibitor core needed to occupy the same spatial region as the two methyl groups present in isoxazole-containing **1** in order to exhibit potent EZH2 inhibition. Consistent with this hypothesis, biochemical potency attenuation relative to **2a** and **2b** was observed for the truncated hydroxymethyl compounds **4a** and **4b** (ethyl to methyl; methoxy to hydroxymethyl, **Table 1**). Interestingly, however, compound **4a** displayed anti-EZH2 biochemical and cell potencies that were within 2-fold of those exhibited by **2a**, suggesting that locating the hydroxyl group further away from the bicyclic lactam core could favorably impact the potency. Accordingly, we prepared an elaborated hydroxyl-containing compound (**5a**) that displayed EZH2 biochemical inhibition and antiproliferation activities that were similar to those exhibited by inhibitors **2a** and **2b**. This outcome, coupled with the cell potency results observed for **4a**, suggested that a hydroxyl group could indeed be accommodated in the EZH2 inhibitor binding site if positioned in an appropriate location relative to the bicyclic lactam core. The significantly weakened activity of the enantiomers corresponding to **3a**, **4a**, and **5a** (**3b**, **4b**, and **5b**, respectively) also indicated that the stereochemistry of these hydroxyl-containing molecules' sp^3 centers played a more important role in maintaining potency relative to what was observed for the related methoxy-containing inhibitors (cf., compounds **2a** and **2b**, **Table 1**). Importantly, compound **5a** also exhibited improvements in HLM stability parameters relative to **2a/b** that likely resulted from the former compound's significantly lower $\log D$ value.

Encouraged by the improved HLM stability and LipE parameters exhibited by **5a**, we enlarged the ethyl moiety

present in the compound via the incorporation of a tetrahydrofuran ring into the inhibitor design. This alteration reduced $\log D$ by 0.8 units relative to **5a** and introduced a second stereocenter into the resulting molecules. Non-stereospecific synthesis afforded four unique entities following achiral and chiral purifications of the initial compound mixture (compounds **6a–d**). As shown in **Table 1**, two of the four compounds prepared (**6a** and **6b**) exhibited very potent EZH2 biochemical and cellular inhibition that were comparable to those displayed by compound **1**. These inhibitors presumably made additional favorable contacts with the EZH2 enzyme relative to molecules **2–5**, and the oxygen atoms contained in the new entities maintained favorable overall lipophilicity values ($\log D = 2.0\text{--}2.1$). Somewhat unexpectedly, however, the absolute configuration of the sp^3 center adjacent to the bicyclic lactam core in the potent **6a** was determined to be opposite that of the corresponding sp^3 center present in the potent truncated compound **4a**. This apparent discrepancy will be explored in greater detail below as part of the cocrystal structure discussion. As expected given their lower $\log D$ values and improved biochemical potency relative to **1**, **6a** and **6b** also exhibited improved HLM stability and LipE parameters (by about two units, **Figure 3**). However, the increased polarity and

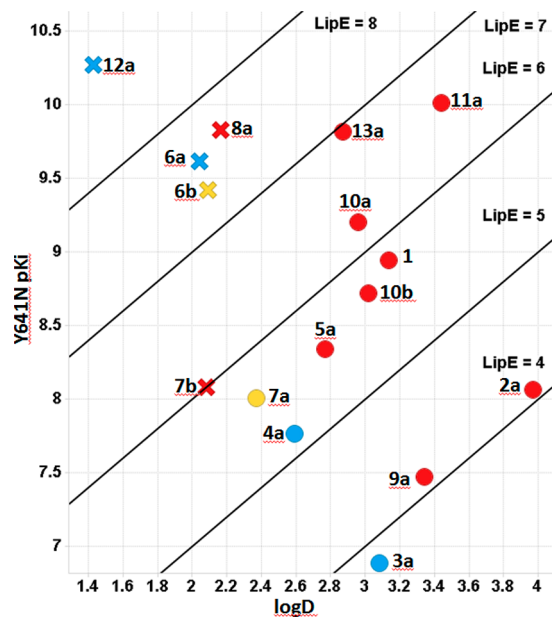


Figure 3. LipE and HLM clearance/permeability comparison of compounds depicted in **Table 1**. Symbols indicate binned compound permeability (MDCK-LE): (×) $\text{MDCK-LE} < 5 \times 10^{-6}\ \text{cm}/\text{s}$; (○) $\text{MDCK-LE} > 5 \times 10^{-6}\ \text{cm}/\text{s}$. Colors indicate binned compound HLM clearance (HLM CL):^{25b} blue, low; yellow, moderate; red, high. The $\log D$ was measured at pH 7.4. LipE = $-[\log_{10}(Y641N K_i)] - \log D$.

hydrogen bond donors of **6a/6b** resulted in relatively low in vitro permeability values that were below the threshold typically associated with well-absorbed molecules in vivo ($\text{MDCK-LE} \geq 5 \times 10^{-6}\ \text{cm}/\text{s}$).²⁶ To address this potential liability, we incorporated an alternative isomeric tetrahydrofuran ring into the inhibitor design that might be able to form an internal hydrogen bond with the hydroxyl group present in the compounds (**7a–d**, **Table 1**). Although some of these compounds (**7a** and **7c**) exhibited improved MDCK-LE permeability relative to **6a/b**, none displayed anti-EZH2 activities that were superior to those associated with compound

1. Further expansion of the tetrahydrofuran ring present in compounds **6a–d** and **7a–d** afforded tetrahydropyran-containing inhibitors **8a** and **8b**. This transformation also removed the tetrahydrofuran stereocenter and thereby reduced the number of compounds that were prepared and separated. Compound **8a** displayed promising EZH2 biochemical and cell-based inhibition that was similar to that exhibited by compound **1**. However, without the intramolecular hydrogen bond present in tetrahydrofuran-containing inhibitors such as **7a** and **7c**, both **8a** and **8b** exhibited unacceptable permeability values in the MDCK-LE assessment.

We also explored whether modification of the ethyl substituent present in compounds **2a** and **2b** could lead to the desired improvements in inhibitor potency. As shown in Table 1, truncation of this ethyl moiety resulted in 4- to 5-fold loss of anti-EZH2 activity (compare **9a** and **9b** with **2a/2b**). This result paralleled the outcomes observed when the methoxy group present in **2a/2b** was truncated (cf., compounds **3a/3b** above) and was consistent with the need for the new compounds to occupy the same spatial region as the two isoxazole methyl groups present in **1** in order to exhibit potent EZH2 inhibition properties (see Figure 2). In contrast, expansion of the ethyl group present in **2a/2b** via incorporation of a tetrahydrofuran ring afforded several molecules with excellent anti-EZH2 properties that were comparable to those exhibited by compound **1** (**10a** and **10b**, Table 1). These inhibitors also exhibited significantly improved in vitro permeability values relative to those displayed by the analogous hydroxyl-containing compounds (compare MDCK-LE data for **10a–d** with **6a–d**, Table 1). However, inhibitors **10a–d** were all relatively labile in the in vitro metabolic stability assessments which precluded further progression of the compounds. Additional expansion of the tetrahydrofuran ring present in **10a–d** via incorporation of a tetrahydropyran moiety did not afford meaningful cell potency improvements (compare **11a** with **10a**). As this change unproductively increased the lipophilicity of the inhibitor series and decreased the kinetic solubility (Table 1), additional exploration of related tetrahydropyran-containing compounds was not performed.

Several piperidine moieties were then incorporated into the inhibitor design as alternatives to the tetrahydropyran (THP) moiety. These piperidine entities were envisioned to occupy space in a manner similar to the THP groups but also imparted lower log *D* values to the resulting lactam inhibitors. As shown in Table 1 and Figure 3, almost all of these new entities displayed either improved or similar EZH2 inhibitory potency and LipE values relative to **1**. However, **12a** suffered from poor permeability and **13a** displayed metabolic instability. Importantly, all of the compounds depicted in Table 1 displayed acceptable kinetic solubility values, supporting our design strategy to improve solubility by replacing the dimethylisoxazole with the sp³-containing, nonaromatic, moieties in the lactam inhibitor series. In addition, the thermodynamic solubility of compound **4a** determined using a crystalline form of the material was significantly superior to that exhibited by compound **1** (**4a** = 34 µg/mL vs **1** = 2 µg/mL, in water with 0.5% CMC and 0.1% polysorbate 80 at 25 °C). This result provided confidence that continued optimization of the bicyclic lactams bearing a 7-position sp³-carbon atom could afford molecules that addressed the key concerns associated with compound **1**.

From analysis of the data for the compounds described in Table 1, it became apparent that the unfavorable HLM stability

exhibited by compound **1** could be significantly improved while retaining potent anti-EZH2 activity. However, these enhancements typically resulted in the simultaneous erosion of in vitro permeability properties for many of the compounds in Table 1 (e.g., compare inhibitors **6a**, **12a** with **1**). As alterations in lipophilicity frequently impact these in vitro parameters in an opposing manner (i.e., increasing log *D* often increases permeability but decreases metabolic stability), we assessed the relationship between these in vitro outcomes and the calculated compound lipophilicity to better understand and define these relationships for the lactam-containing EZH2 inhibitor series. Analysis of previously prepared compounds bearing aromatic (i.e., sp²-containing) or phenoxy (sp³-containing) R moieties appended to 7-position of the bicyclic lactam core indicated that those with calculated log *D* (clogD) values in excess of 2.9 were much less likely to afford favorable in vitro metabolic stability properties relative to molecules that were below this cutoff (Figure 3S in Supporting Information). Similar comparison of clogD values with measured MDCK-LE data suggested that inhibitors with clogD greater than 1.5 would be more likely to display acceptable in vitro permeability outcomes (Figure 3S, Supporting Information). An analysis of the joint probability of observing a molecule that is simultaneously permeable and metabolically stable as a function of clogD (Figure 3S, Supporting Information) revealed an improved likelihood of a favorable outcome for ligands with a clogD in the range of 1.5–2.9. Subsequent compound designs were prioritized to lie within this clogD range. When combined with the ligand-based inhibitor design strategy described at the beginning of this work, we anticipated that this physicochemical property-based design approach would improve the chances of identifying potent EZH2 inhibitors that also displayed superior LipE and reasonable in vitro ADME profiles.

With the above strategies in mind, we revisited our exploration of utilizing piperidines as replacements for the dimethylisoxazole moiety present in compound **1**. Our prior studies with lactam-containing compounds related to **1** demonstrated that a 4-methoxy-6-methylpyridone²¹ could substitute for the 4,6-dimethyl analog typically present in many EZH2 inhibitors without potency loss (e.g., **14**, Table 2, compare to **1**). Accordingly, we frequently utilized this alternative pyridone fragment during our resumed optimization efforts as one means of modulating compound lipophilicity into the desired range. Such introduction typically reduced calculated log *D* values by 0.2–0.5 units relative to incorporation of the 4,6-dimethylpyridone moiety with larger differences sometimes noted in measured log *D* parameters. Several new piperidine-containing compounds incorporating either 4,6-dimethylpyridone or 4-methoxy-6-methylpyridone were designed to modulate the pK_a of **12a** (**15a/15b**) or to reduce the log *D* of **13a** (**16a/16b**, **17a/17b**). As shown in Table 2, some of these compounds displayed potent EZH2 inhibition (**15a**, **16a**, and **17a**) and one (**16b**) exhibited the desired combination of favorable HLM stability and in vitro permeability outcomes. Encouragingly, incorporation of various sulfones into the inhibitor design in lieu of the piperidine moiety afforded several molecules with anti-EZH2 activities comparable to those of compound **1**, improved in vitro stability properties, and acceptable MDCK-LE values (e.g., **18a** and **19a**). However, extension of the methoxy group present in **19a** to a larger ethoxy moiety resulted in erosion of anti-EZH2 inhibitory properties (compounds **20a/20b**). We also briefly explored the use of heterocycles as piperidine replacements

Table 2. Influence of R and R' Substitutions on log D, Potency, and ADME Properties^e

Cpd# ^a	R'	R	Y641N biochem. K _i (nM) ^b	Karpas422 cell H3K27me3 IC ₅₀ (nM) ^c	Karpas422 cell Prolif. IC ₅₀ (nM) ^c	HLM (μ L/min/ mg protein)	MDCK- LE (X10 ⁻⁶ cm/sec)	logD ^d / (clogD)	Sol. (μ M)
14	OMe		0.15	8	27	70	11	2.7 (2.6)	384
15a (+)	Me		0.64	16	25	72.7	7	2.7 (2.2)	523
15b (-)	Me		530	1313	2256	78.3	7.9	2.8 (2.2)	519
16a (+)	Me		0.25	13	21	42	7.3	2.2 (2.1)	508
16b (-)	Me		70	749	3140	23	7.1	2.3 (2.2)	513
17a (+)	OMe		0.13	15	10	25.6	1.5	1.7 (1.9)	480
17b (-)	OMe		25	231	250	12.6	1.1	1.7 (1.9)	453
18a (+)	Me		0.35	18	24	40	6.3	2.2 (2.2)	373
18b (-)	Me		93	430	970	15	5.7	2.2 (2.2)	415
19a (+)	Me		0.22	9	24	52.5	5.3	1.9 (1.9)	161
19b Ent 19a (ND)	Me		640	3107	4829	23	6.1	1.9 (1.9)	159
20a (+)	Me		2.9	62	34	124	12	2.4 (2.2)	453
20b Ent 20a (ND)	Me		460	6084	5555	45.7	7.7	2.3 (2.2)	446
21a (+)	Me		24	273	122	21.2	5.8	2.0 (2.1)	596
21b (-)	Me		360	7958	2486	22.7	8.6	2.0 (2.1)	481
22a (+)	OMe		<0.1	4	9	60	7.2	2.5 (2.0)	433
22b (ND)	OMe		0.19	16	24	66.9	7.2	2.5 (2.1)	439
22c Ent 22a (-)	OMe		42	110	113	97.2	8.4	2.5 (2.1)	521
22d Ent 22b (-)	OMe		92	391	269	75	8.2	2.4 (2.0)	505
23a (+)	OMe		<0.1	4	6	39	4.8	1.9 (1.8)	538
23b (-)	OMe		16	75	467	17	6.8	1.6 (1.9)	543
24a (+)	OMe		0.7	8	9	206.6	5.7	2.3 (2.3)	486
24b (-)	OMe		350	253	559	168	4.8	2.2 (2.3)	512
25a (+)	OMe		1.5	99	108	<8	0.7	1.4 (1.3)	234
25b (-)	OMe		1500	>32000	10599	<7	1.2	1.3 (1.4)	582

^aAll compounds bearing chiral centers are single stereoisomers. To help depict enantiomeric pairs, the sign of the optical rotation is

Table 2. continued

provided below compound number. ^b K_i values are geometric mean values from at least three independent experiments. For each experiment, K_i values are determined from 11-point dose-response curves with each dose performed in duplicate. ^cUnless otherwise indicated, the reported IC₅₀ values are the geometric mean of values from two independent experiments. ^dThe log D was measured at pH 7.4. ^eND: not determined.

(e.g., the isoxazole present in 21a/21b). However, the incorporation of such entities typically resulted in significant potency loss (compared with 6a/6b, 7a/7b, and 8a in Table 1).

In pursuit of EZH2 inhibitor potency superior to compound 1, we also applied our ligand-based and property-based design strategies to the generation of new inhibitors that contained various cyclic ethers in their chemical structures. On the basis of the outcomes observed for related entities during our initial efforts, we anticipated that the new molecules might exhibit very potent anti-EZH2 inhibition properties (cf., compounds 6a/6b, 8a, 10a/10b; Table 1). A comparison of the lipophilic metabolism efficiency (LipMetE)³¹ of 6a (0.7), 8a (0.6), and 10a (0.9) indicated that 10a displayed the best LipMetE value among all three analogs and therefore represented a good starting point for further log D reduction. Therefore, in order to improve the metabolic stability for 10a, we utilized the 4-methoxy-6-methylpyridone moiety to replace the 4,6-dimethylpyridone present in 10a. This transformation afforded compounds 22a–d that possessed calculated log D values between 2.0 and 2.1. As expected, these compounds generally exhibited improved in vitro HLM clearance outcomes relative to the 10a–d analogs which incorporated the more lipophilic 4,6-dimethylpyridone moiety (cf., Table 1). In spite of these enhancements, however, the absolute in vitro HLM clearance values for 22a–d were not sufficiently low to support further advancement of the compounds (target of \leq 30 (μ L/min)/mg protein). These outcomes were consistent with the property-based analysis described above in which approximately 53% of the molecules with optimal calculated log D values (1.5–2.9) did not exhibit the desired in vitro stability properties. In the case of compounds 22a–d, the corresponding measured log D values were somewhat higher than the calculated parameters (Table 2), and this increased actual vs calculated lipophilicity likely contributed to the undesired in vitro stability.

Accordingly, we decided to further reduce the clogD of new designs containing related cyclic ethers by another 0.5 units in order to further improve in vitro metabolic stability relative to compounds 22a–d. This approach led to introduction of an oxetane ring into the inhibitor series as a replacement for the tetrahydrofuran moiety present in several other potent molecules. This transformation afforded compounds 23a/23b which displayed improved in vitro HLM clearance values relative to both 22a–d and the dimethylisoxazole-containing lead compound 1. This modification also removed a chiral center from the tetrahydrofuran-containing structures such as 22a–d and thereby simplified the molecular complexity associated with the new (sp^3 -center containing) inhibitors. Importantly, the more potent enantiomer (23a) exhibited biochemical and cell-based EZH2 inhibition activities that were superior to those displayed by compound 1 and all other analogs in this lactam series along with acceptable in vitro permeability and good kinetic solubility properties. The absolute configuration of 23a was determined by small

molecule crystal structure to be the same as that present in the potent tetrahydrofuran-containing inhibitor **6a** described above (Table 1). This result suggested that the tetrahydrofuran and oxetane rings present in the corresponding inhibitors occupied similar regions of the EZH2 binding pocket (more details regarding such interactions are provided in the cocrystal structure discussion below). A methyl group was also added to the oxetane present in **23a/23b** thereby affording **24a/24b** to explore the impact on potency and metabolic stability. As shown in Table 2, potent cellular EZH2 inhibitory activity was retained in one of the resulting enantiomers (**24a**). However, the in vitro stability parameters of the new molecules were dramatically eroded (compare **24a/24b** with **23a/23b**, Table 2). Similar replacement of the methoxy group adjacent to the oxetane in **23a/23b** with a hydroxy moiety resulted in unfavorably low calculated log D values and unacceptable measured in vitro permeability outcomes (**25a/25b**; clogD = 1.3).

We found that emphasizing ligand designs in the clogD range of 1.5–2.9 was a useful component of our optimization strategy as it successfully afforded several new compounds with improved HLM stabilities relative to compound **1** and acceptable in vitro permeability properties. These molecules also typically exhibited LipE values that were significantly superior to that of **1** indicating that potency improvements in the new series were achieved with adequate control of molecular lipophilicity (Figure 4). Unfortunately, and for

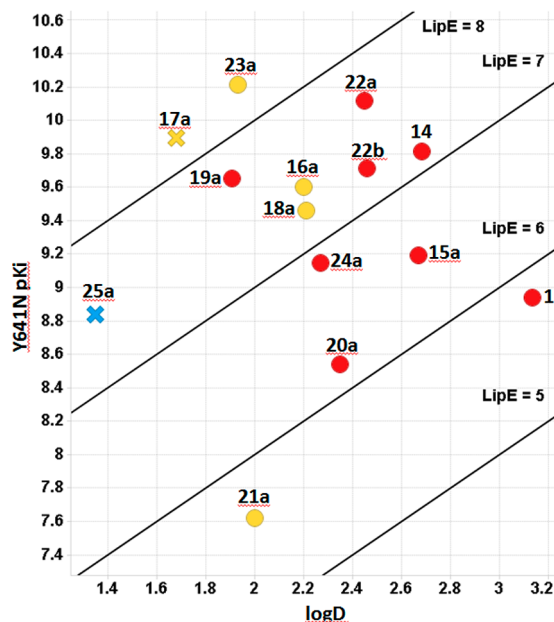


Figure 4. LipE and HLM clearance/permeability comparison of compounds depicted in Table 2. Symbols indicate binned compound permeability (MDCK-LE): (x) $MDCK-LE < 5 \times 10^{-6} \text{ cm/s}$; (○) $MDCK-LE > 5 \times 10^{-6} \text{ cm/s}$. Colors indicate binned compound HLM clearance (HLM CL):^{25b} blue, low; yellow, moderate; red, high. The log D was measured at pH 7.4. LipE = $-[\log_{10}(Y641N K_i)] - \log D$.

unknown reasons, the more biologically potent compound among a given enantiomer pair was almost invariably also less stable in the in vitro HLM experiments. Among all the molecules depicted in Tables 1 and 2, compound **23a** displayed the best combination of EZH2 inhibitory activity, lipophilic ligand efficiency (LipE), in vitro metabolic stability, and

permeability characteristics. Although the compound's in vitro HLM stability was slightly higher than our initial target value (39 vs 30 ($\mu\text{L}/\text{min}$)/mg protein), the molecule exhibited more favorable stability in the in vitro human hepatocyte assessments that were significantly improved relative to those observed for compound **1** (12 vs 75 ($\mu\text{L}/\text{min}$)/million cells). In addition, the thermodynamic solubility of a crystalline form of the compound was dramatically superior to that exhibited by compound **1** (**23a** = 315 $\mu\text{g}/\text{mL}$ in water with 0.5% CMC and 0.1% polysorbate 80 at 25 °C). Compound **23a** also displayed longer residence time relative to **1**. The biochemical half-lives for target engagement of **23a** were determined to be about 22 and 6 h against the wild type and Y641N mutant of EZH2, respectively (Figure 1S, Supporting Information). These collective properties suggested that **23a** might overcome the liabilities that prevented progression of **1** into development, and **23a** was therefore advanced into in vivo studies to further define this potential.

As shown in Figure 5A and Figure 5B, twice-daily oral administration of crystalline **23a** suspension formulation to mice bearing Karpas-422 DLBCL tumor xenografts (which contain the Y641N EZH2 mutation) resulted in significant inhibition of tumor growth (100 mg/kg dose) or tumor regression (300 mg/kg) with minimal impact on animal body weights. Even more profound tumor regression outcomes were observed when **23a** was dosed subcutaneously once-daily at the 100 mg/kg level (Figure 5A). This profound tumor regression effect was also sustained for another 40 days after the termination of the treatment on day 31. Importantly, analysis of samples collected on day 9 of the in vivo experiment 4 h after the last dose was administered showed significant reductions in H3K27me3 levels in all tumors treated with compound **23a** (Figure 5C). In the case of the subcutaneous dosing arm, strong day 9 reductions in tumor H3K27me3 levels correlated well with the observed tumor regressions (compare Figure 5A and Figure 5C). The intermediate levels of H3K27me3 reductions noted in the oral dosing arms relative to the subcutaneous group also correlated with the corresponding efficacy results (i.e., both oral arms afforded fewer H3K27me3 reductions and efficacy outcomes relative to the 100 mg/kg sc group). For reasons that are not understood at this time, analysis of the day 9 H3K27me3 tumor levels did not correlate well with the disparate long-term efficacy results observed for the two oral dosing arms. However, the tumor growth inhibition (TGI) plots corresponding to these two oral dosing groups were not well-separated at the day 9 juncture, and it is possible that additional sampling of the H3K27me3 pharmacodynamic marker beyond the day 9 time point would provide further insights into these long-term outcomes.

We also assessed the pharmacokinetic properties of compound **23a** in the tumor-bearing mice so as to better define the plasma exposures associated with strong pharmacodynamic and efficacy impacts. As shown in Figure 5D, twice-daily oral administration of 300 mg/kg **23a** afforded free mouse plasma levels that exceeded the compound's measured in vitro Karpas-422 antiproliferation IC₉₀ value for approximately 24 h (IC₉₀ = 60 nM). In contrast, similar oral dosing of **23a** at the 100 mg/kg level resulted in lower free exposures that fell below this cell IC₉₀ threshold sometime during the 7–24 h portion of the two-dose administration cycle. These exposure differences correlated with the different long-term efficacy results observed for the two oral dosing groups (Figure 5A, lower exposure = less TGI after day 35). This correlation suggested that

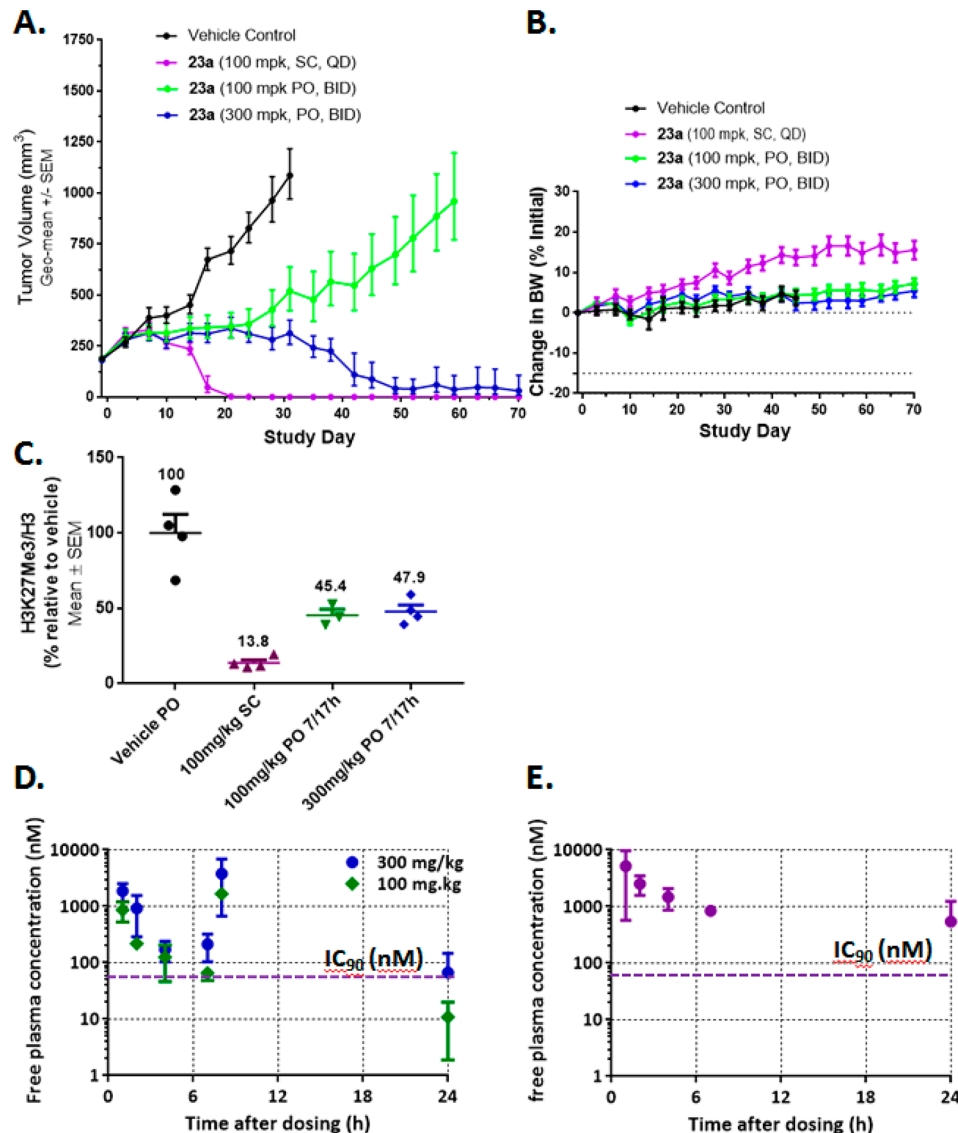


Figure 5. PK/TGI relationship for 23a in Karpas-422 xenograft model: (A) tumor growth inhibition graph for all treatment groups; (B) body weight measurement; (C) H3K27me3 reduction for all treatment groups at day 9 (4 h after last dose); (D) plasma exposure of 23a po 7 h/17 h b.i.d. dosing; (E) plasma exposure of 23a sc q.d. dosing.

continuous and near-complete suppression of EZH2 activity (approximated by maintaining free inhibitor levels in excess of cellular antiproliferation IC_{90} values) was required to afford meaningful long-term TGI outcomes in the Karpas-422 model. In support of this hypothesis, free mouse plasma exposures of 23a associated with the subcutaneous dosing arm (for which tumor regressions were observed) were even greater than those determined for either oral dosing group (Figure 5E). The subcutaneous dosing likely bypassed the first-pass clearance of 23a in mice (mouse hepatocytes clearance = 60.1 ($\mu\text{L}/\text{min}$)/million cells) and thus resulted in the high exposures relative to the oral dosing groups. Additional low-dose (2 mg/kg) PK studies in rats showed that the in vivo intravenous clearance was hepatic-blood-flow-limited (\sim 70 (mL/min)/kg). This result was consistent with in vitro metabolic clearance in rat hepatocytes (109 ($\mu\text{L}/\text{min}$)/million cells).

Compound 23a was profiled in the CEREP histone methyltransferase and broad-ligand screening panels along with kinase panel (Life Technologies) and was shown to be a highly selective EZH2 inhibitor (Tables 1S, 2S, and 3S in

Supporting Information). The only other methyltransferase showing significant inhibition was EZH1. The K_i for EZH1 was determined to be 70 nM (Figure 2S) compared to a K_i of <0.1 nM for EZH2. In addition, the compound did not impair the function of various cytochrome P450 (CYPs) isoforms when tested in vitro against these enzymes (IC_{50} values of $>30 \mu\text{M}$ for CYP 1A2, 2C8, 2C9, 2C19, 2D6, and 3A4). The molecule also did not exhibit appreciable inhibition of the human ether-à-go-go-related gene (hERG) ion channel ($\text{IC}_{50} > 100 \mu\text{M}$) and was negative in Ames and micronucleus in vitro assessments of genotoxicity. These favorable properties, along with the encouraging in vivo PK and efficacy data described in this work and several other attributes that will be described elsewhere, enabled the selection of compound 23a as a clinical development candidate (PF-06821497). Further details regarding related development activities and the clinical characterization of the molecule will be reported in subsequent disclosures. Importantly, 23a displayed superior LipE among all analogs synthesized in the lactam series. This superior LipE enabled the combination of excellent potency, sufficient

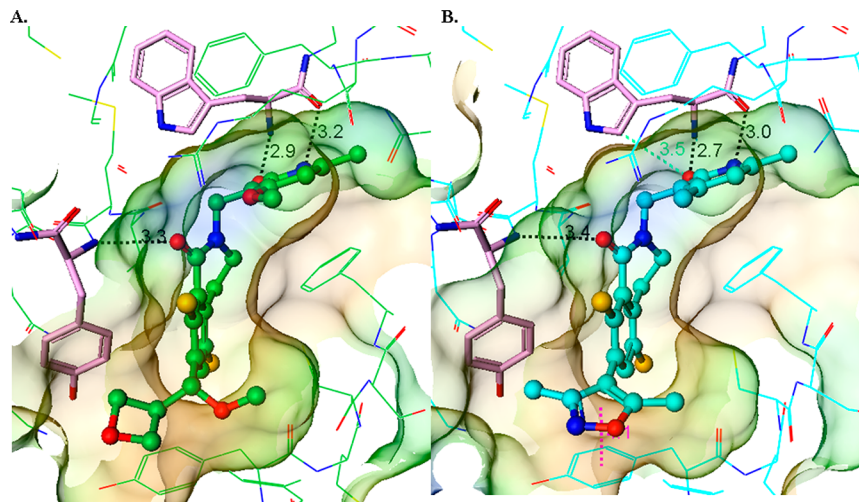


Figure 6. (A) Cocrystal structure of compound 23a in complex with EZH2 (2.8 Å, PDB code 4W2R). (B) Cocrystal structure of compound 1 in complex with EZH2 (3.0 Å, PDB code 6B3W). EZH2 residues involved in key interactions with 23a or 1 are depicted in pink.

Table 3. Calculated MM-GBSA Binding Energy (ΔE) and Components^a

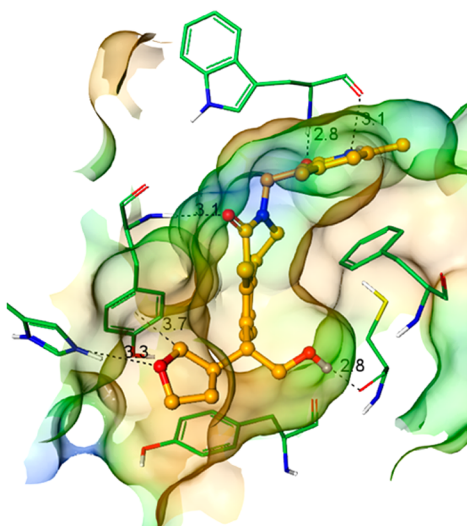
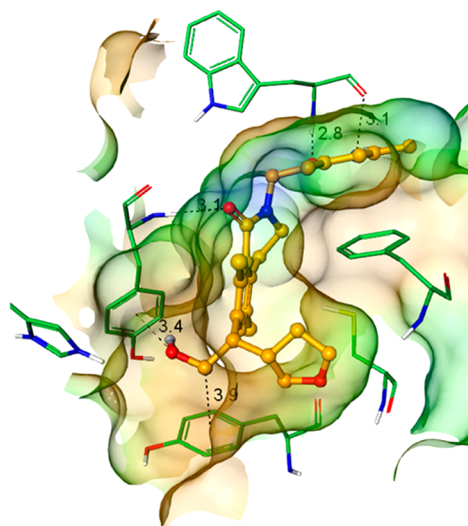
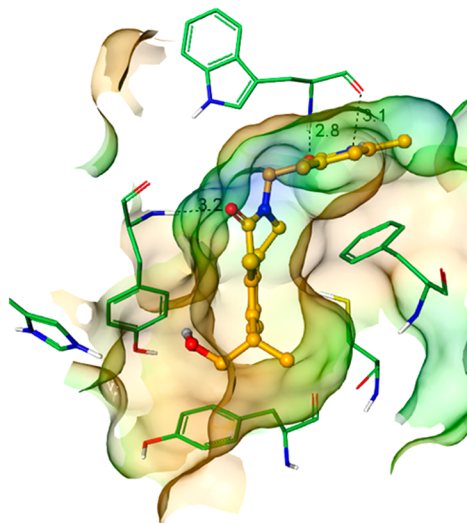
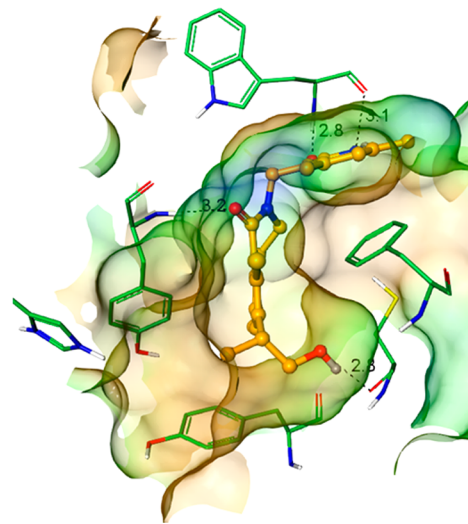
compd	MM-GBSA binding energy components					calcd ΔE	calcd relative ΔE	exptl ΔG
	electrostatic	van der Waals	desolvation (GBSA)	ligand strain	protein strain			
23a	-47.1	-59.2	42.8	1.9	4.7	-56.8	0.0	-13.6
6a	-45.2	-58.0	42.5	1.9	3.1	-55.8	1.0	-13.1
14	-43.3	-59.0	40.7	2.0	5.2	-54.5	2.3	-12.9
1	-38.1	-58.8	37.0	2.1	5.0	-52.9	3.9	-12.1
23b	-35.8	-58.2	34.3	3.3	4.0	-52.5	4.3	-10.6
6c	-39.2	-62.8	40.0	2.7	8.2	-51.0	5.8	-8.0
4a	-38.4	-53.8	37.1	1.3	3.8	-50.1	6.7	-10.6
25a	-43.6	-55.1	42.7	1.9	4.1	-50.0	6.8	-12.0
4b	-36.9	-51.1	35.3	1.6	1.8	-49.4	7.4	-8.9
25b	-37.3	-56.0	38.4	3.6	2.9	-48.4	8.4	-9.2

^aAll units in kcal/mol.

metabolic stability, permeability, and solubility properties. Specifically, the good thermodynamic solubility and acceptable permeability provided prediction of sufficient absorption for an oral drug to treat EZH2-related diseases.

After 23a was selected for advancement into development, we obtained a cocrystal structure of the compound with the PRC2 complex consisting of engineered *Anolis carolinensis* (American chameleon) EZH2, human EED, and the VEFS domain of human Suz12 proteins as described previously.³² This structure enabled understanding of the key features required for optimal binding of the lactam inhibitors to EZH2. A related cocrystal structure of compound 1 with the identical EZH2-containing three protein complex was also obtained in order to better understand the improved potency of 23a compared to 1. As depicted in Figure 6A, the 4-methoxy-6-methylpyridone group of 23a formed hydrogen bond interactions with the backbone carbonyl and amide NH moieties of Trp624 (Figure 6A). Similar interactions were observed between the EZH2 and the 4,6-dimethylpyridone moiety present in compound 1 (Figure 6B).³³ This region of the EZH2 binding site is known to accommodate a portion of the S-adenosyl-L-methionine (SAM) cofactor involved in the methyl transfer reaction catalyzed by the enzyme.^{34,35} Binding of pyridone-containing inhibitors such as 1 and 23a to EZH2 likely disrupts the ability of SAM to associate with the protein and thereby impairs the enzyme's biological function.

The 4-methoxypyridone substituent of 23a bound somewhat more favorably in the EZH2 binding pocket relative to the corresponding 4-methylpyridone group of 1, and this difference may account for some of the subtle potency improvements observed for inhibitors described above that incorporated the former fragment in place of the latter (e.g., compare 22a with 10a and 17a with 16a, Tables 1 and 2). The carbonyls of the lactam cores in both 23a and 1 formed hydrogen bonds with the backbone NH of EZH2 Tyr111 (Figure 6A and 6B). As expected based on the ligand design strategy pursued above, the sp³-containing oxetane-methoxy group (R group) of 23a occupied the same space as the dimethylisoxazole of 1. A potential donor-π interaction between the partially polarized oxetane ring hydrogens and the EZH2 Tyr111 side chain was also observed in the 23a cocrystal structure. This interaction, which may contribute on the order of 0.5 kcal/mol (relative to the methyl group forming a corresponding aliphatic interaction in 1),³⁵ and the pyridone substituent changes mentioned above are expected to account for at least some of the anti-EZH2 potency differences observed for these two inhibitors. MM-GBSA calculations (see Supporting Information) were able to correctly rank this pair of compounds and therefore provided the opportunity to gain some additional insights into the binding affinity differences. Energy components from these calculations suggest that the potency improvement observed for 23a can be primarily attributed to a significant increase in

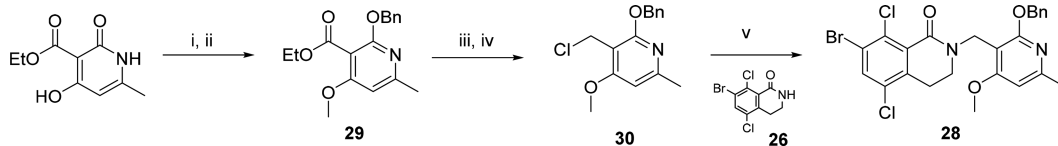
A. Modeled 6a**B. Modeled 6c****C. Modeled 4a****D. Modeled 4b****Figure 7.** Optimized MM-GBSA models for stereochemical ligand pairs **6a/6c** and **4a/4b**.

favorable electrostatic interactions between the ligand and the protein while being partially attenuated by a corresponding increase in the desolvation penalty (Table 3).

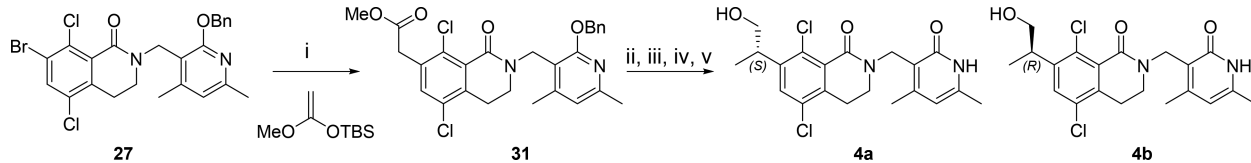
The 23a-PRC2 cocrystal structure also provided useful insights regarding the reason for the stereochemistry switch associated with the active enantiomers **4a** and **6a** and the difference in binding affinities between the stereoisomers **6a/6c** and **4a/4b**. Computational modeling of the enantiomeric tetrahydrofuran-containing inhibitors **6a** and **6c** into the EZH2 binding pocket revealed a strong energetic preference for the *R,R*-isomer, **6a** (Figure 7A and Figure 7B; Table 3). For all stereoisomeric pairs of compounds modeled, the best-scoring binding poses from automated protein–ligand docking oriented the R-group so that the methine hydrogen was syn to the adjacent chloro group, thereby avoiding the allylic 1,3-strain present in the significantly higher-energy conformations.³⁶ This conformational constraint resulted in the exchange of the hydroxymethyl and tetrahydrofuran groups within the protein binding pocket. MM-GBSA calculations correctly ranked the potencies of **6a** and **6c**, and an analysis of the

energy components indicated that the potency differences were primarily due to more favorable protein–ligand electrostatic interactions for compound **6a** along with an increase in protein and ligand strain for **6c** (Table 3).

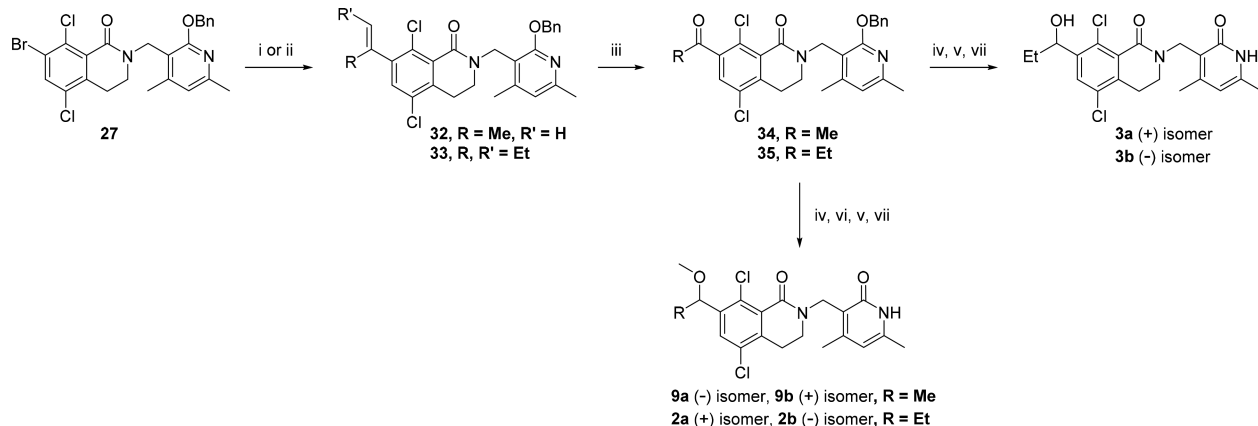
It is noteworthy that for the smaller R-group in the **4a/4b** pair, the *S*-isomer was observed to be more potent. Modeling studies predicted that the hydroxyl group in the more potent ligand, **4a**, would bind analogously to the less potent compound, **6c** (compare Figure 7B and Figure 7C). Although the MM-GBSA calculations correctly rank the binding affinities for this ligand pair, the predicted energy difference is small (Table 3). The slightly improved van der Waals and electrostatic interactions for **4a** are largely offset by an increase in protein strain and desolvation leading to this small predicted difference in potency. The marginal improvement in the electrostatic binding component may appear counterintuitive given the hydrogen bond present in **4b** but absent in the **4a** model; however, the relatively poor geometry³⁷ (Figure 7D) observed for this interaction suggests that its contribution should be small.

Scheme 1. Synthesis of 4-Methoxy-6-methylpyridine Template 28^a

^aReagents and conditions: (i) BnBr, Ag_2CO_3 , THF, 60 °C, 62%; (ii) MeI, K_2CO_3 , DMF, 89%; (iii) LiAlH_4 , THF, 0–25 °C, 97%; (iv) SOCl_2 , EtOAc , 0 °C, 95%; (v) 26, $\text{KO}'\text{Bu}$, EtOAc , 75 °C, 81%.

Scheme 2. Representative Synthetic Route of Primary Alcohols^a

^aReagents and conditions: (i) $[(t\text{-Bu})_3\text{P}]_2\text{Pd}$, LiF, DMF, 61%; (ii) CH_3I , NaH , DMF, 0 °C, 56%; (iii) LiBH_4 , THF, 50 °C, 79%; (iv) TFA, DCM; then K_2CO_3 , MeOH , 99%; (v) chiral SFC, (S)-isomer 4a, 42%; (R)-isomer 4b, 40%.

Scheme 3. Synthesis of Secondary Alcohols and Ethers 2a, 2b, 3a, 3b, 9a, and 9b^a

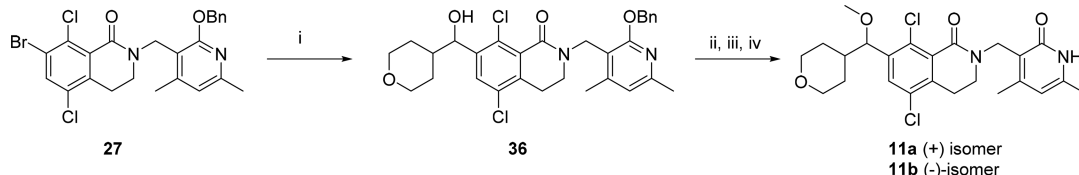
^aReagents and conditions: (i) isopropenylboronic acid pinacol ester, $\text{Pd}(\text{dppf})\text{Cl}_2$ -DCM, Na_2CO_3 , dioxane, 70 °C, 66%; (ii) (Z)-3-hexenyl-3-boronic acid catechol ester, CsF , $\text{Pd}(\text{PPh}_3)_4$, dioxane, 100 °C, 88%; (iii) ozone, DCM, -70 °C, 67–94%; (iv) NaBH_4 , MeOH ; (v) TFA, DCM; (vi) $\text{KO}'\text{Bu}$, MeI , DMF ; (vii) chiral SFC.

CHEMISTRY

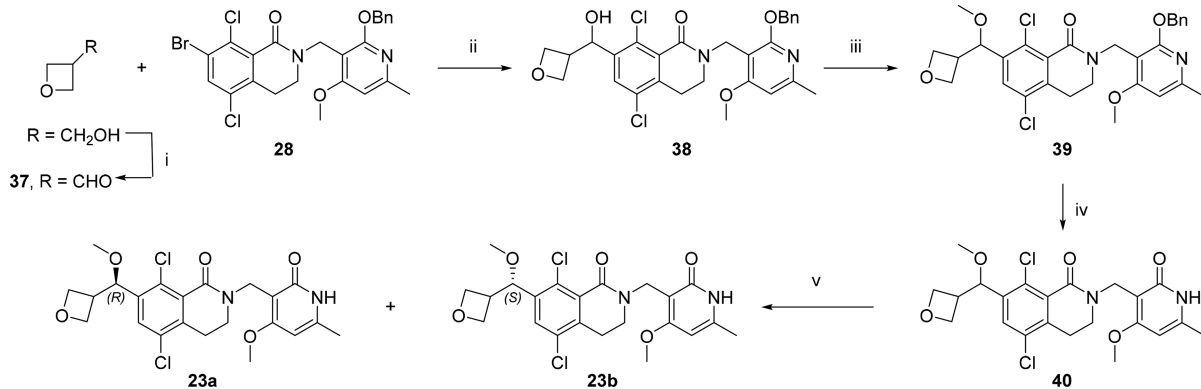
Synthesis of the Templates. The syntheses of 7-bromo-5,8-dichloro-3,4-dihydroisoquinolin-1(2*H*)-one 26 and the 4,6-dimethylpyridine-containing bromide template 27 were described in an earlier publication.²⁴ The synthesis of bromide template 28, which featured the 4-methoxy-6-methylpyridine side chain, began with regioselective alkylation of commercially available ethyl 2,4-dihydroxy-6-methylnicotinate at the 2-hydroxy moiety using benzyl bromide in the presence of Ag_2CO_3 at 60 °C (Scheme 1).³⁸ The silver carbonate directed O-alkylation was selected as a deliberate synthesis strategy since O-debenzylation of the alkylated 2-pyridone was expected to be a facile process using TFA. In contrast, deprotection of *N*-benzyl 2-pyridone would likely require more forcing or hydrogenolysis conditions³⁹ which might cause cleavage of the aryl chlorides. Alkylation of the 2-OBn intermediate with methyl iodide in the presence of K_2CO_3 gave methyl ether 29. Lithium aluminum hydride reduction of the ethyl ester followed by chlorination of the benzyl alcohol with thionyl chloride afforded the alkyl chloride 30. Finally, N-alkylation of 26²⁴ using $\text{KO}'\text{Bu}$ in EtOAc provided 28. Templates 27 and 28

were further elaborated by the following methods to produce the test compounds 2a/2b through 25a/25b.

Synthesis of Primary Alcohols. To synthesize primary alcohol analogs 4a/4b, 5a/5b, 6a–d, and 8a/8b, the 4,6-dimethylpyridine template 27 was functionalized with a $\text{CH}_2\text{CO}_2\text{Me}$ group at the 7-position of the dihydroisoquinolinone to serve as a flexible handle for incorporation of sp^3 -containing side chains (Scheme 2). Using modified Hartwig α -arylation conditions,⁴⁰ the lithium enolate of methyl acetate, prepared in situ using *tert*-butyl((1-methoxyvinyl)oxy)-dimethylsilane and LiF, was coupled with 27 in a reaction catalyzed by $(t\text{-Bu}_3\text{P})_2\text{Pd}$. These α -arylation conditions afforded ester 31 in 61% yield, setting the stage for introduction of branching R groups. A representative example of this method ($\text{R} = \text{CH}_3$), leading to compounds 4a and 4b, is shown in Scheme 2. The methyl branch was incorporated via alkylation α to the ester using iodomethane and sodium hydride in DMF. Ester reduction using lithium borohydride was followed by acid-catalyzed deprotection of the benzyl group to reveal the 2-pyridone. The racemic mixture was separated using chiral SFC to afford single stereoisomers. The absolute (*R*) stereochemistry of 4b was determined by small-molecule X-ray

Scheme 4. Representative Synthetic Route of Secondary Alcohols and Ethers from Aldehydes^a

^aReagents and conditions: (i) *i*-PrMgCl–LiCl, tetrahydro-2*H*-pyran-4-carbaldehyde, THF, –40 to 0 °C, 46%; (ii) KO^tBu, CH₃I, THF, 0–25 °C, 65%; (iii) TFA, DCM; (iv) chiral SFC; 11a, 35%; 11b, 34%.

Scheme 5. Synthesis of Oxetane Analogs 23a and 23b^a

^aReagents and conditions: (i) PDC, DCM, rt, 26%; (ii) *i*-PrMgCl–LiCl, THF, –65 to –10 °C, 59%; (iii) CH₃I, KO^tBu, THF, 0 °C, 91%; (iv) PtO₂, H₂ (1 atm), EtOAc, rt, 54%; (v) chiral SFC, 36% (R) isomer 23a and 16% (S) isomer 23b.

crystallography. Crystallographic data for 4b are available in the Supporting Information.

Synthesis and characterization of additional analogs made by the method of Scheme 2 (5a/5b, 6a–d, and 8a/8b) are reported in the Supporting Information, as well as an alternative C–H insertion route used to make analogs 7a–d (Scheme S1, Supporting Information).

Synthesis of Secondary Alcohols and Ethers. Synthesis of simple methyl- and ethyl-substituted secondary alcohols and ethers 2a/2b, 3a/3b, and 9a/9b began with a Suzuki–Miyaura cross-coupling reaction of isopropenylboronic acid pinacol ester or (*Z*)-3-hexenyl-3-boronic acid catechol ester on the 4,6-dimethylpyridine template 27 (Scheme 3). Ozonolysis of the alkenes (32 and 33) gave ketones 34 and 35, which were reduced with NaBH₄ in MeOH to afford racemic mixtures of secondary alcohols. At this stage, deprotection of the benzyl group and separation of the racemic mixture by chiral SFC yielded single-enantiomer secondary alcohol analogs 3a and 3b. Alternatively, after reduction of ketones 34 and 35, the resulting racemic alcohol mixtures were converted to methyl ethers (KO^tBu, MeI, DMF). The benzyl groups were then removed and the resulting racemates were separated by chiral SFC to prepare the pyridones 2a, 2b, 9a, and 9b.

More complex sp³-containing side chains were introduced via a turbo Grignard⁴¹ reaction on an aldehyde monomer set. Scheme 4 shows a representative example of this method which led to the synthesis of the THP analogs 11a and 11b. The Grignard reagent was generated from the 4,6-dimethylpyridine template 27 using *i*-PrMgCl–LiCl in THF, and the resulting anion was quenched with tetrahydro-2*H*-pyran-4-carbaldehyde to give racemic secondary alcohol 36. Alkylation of the alcohol with iodomethane/KO^tBu, TFA-promoted deprotection of the benzyl group, and separation of the racemate by chiral SFC

afforded (+)-isomer 11a and (–)-isomer 11b. The absolute stereochemistry for these compounds was not determined.

Synthesis and characterization of additional analogs made by the method of Scheme 4 (10a–d, 18a/18b, 19a/19b, 20a/20b, and 22a–d) are reported in the Supporting Information. A variation of this method using *N*-Boc-4-formylpiperidine as the aldehyde and additional N-functionalization steps after simultaneous Boc and benzyl deprotection by TFA afforded piperidine-containing analogs 12a/12b, 13a/13b, 15a/15b, 16a/16b, 17a/17b. These procedures are described in the Supporting Information.

Due to the chemical sensitivity of the oxetane ring, synthesis of oxetane containing analogs, including 23a, required slightly modified conditions (Scheme 5). Oxidation of commercially available oxetane-3-methanol by pyridinium dichromate (PDC) with minimal workup gave crude oxetane-3-carbaldehyde 37 as a solution in dichloromethane,⁴² which was used immediately in the subsequent Grignard reaction. Metal–halogen exchange of 4-methoxy-6-methylpyridine-containing bromide template 28 was performed using turbo Grignard, and the resultant anion was quenched with crude aldehyde 37. The racemic secondary alcohol thus produced, 38, was alkylated with iodomethane as described before to give racemic ether 39. To avoid acid-catalyzed oxetane ring opening,⁴³ it was necessary to use hydrogenolysis to remove the benzyl group, yielding racemic pyridone 40. The enantiomers were separated using chiral SFC to give 23a and 23b. The absolute stereochemistry of each enantiomer was determined by small-molecule X-ray crystallography. Crystallographic data for 23a and 23b are available in the Supporting Information. Synthesis and characterization of additional oxetane analogs made by the method of Scheme 5 (24a/24b, 25a/25b) are reported in the Supporting Information along with the methods used to

prepare the remaining analogs discussed in this paper (**14**, **21a**/**21b**).

CONCLUSION

A new series of lactam-derived EZH2 inhibitors was designed to improve *in vitro* human metabolic stability and thermodynamic solubility issues associated with the previously described lead compound **1**. In the absence of supporting crystallographic information, several replacements for the dimethylisoxazole group present in **1** were identified that incorporated an sp^3 -hybridized carbon atom attached to the 7 position of the bicyclic lactam inhibitor core. A separate property based design strategy was also employed during the optimization efforts in which correlation of calculated $\log D$ values with *in vitro* measurements of both metabolic stability and permeability identified a clogD range (1.5–2.9) that afforded an increased probability of simultaneously achieving favorable outcomes for these ADME parameters. The ligand-based and property-based design strategies described in this paper led to the identification of an oxetane-containing compound (**23a**) that displayed an adequate overlap of EZH2 inhibitory potency, *in vitro* ADME properties, and physical chemical properties (e.g., thermodynamic solubility). The molecule also displayed robust tumor growth inhibition activity in mouse xenograft models along with strong associated pharmacodynamic effects (such as reduction of H3K27me3 in tumors). Importantly, compound **23a** improved LipE by 2 units relative to lead compound **1** (calculated using enzyme inhibition values) and also enhanced anti-EZH2 cell potency by 5- to 6-fold. This potency improvement, coupled with the observed moderate *in vitro* human microsomal clearance, favorable thermodynamic solubility properties, and strong *in vivo* antitumor efficacy observed in preclinical models, suggested a good potential for compound **23a** to effectively modulate EZH2 activity in human clinical settings. The molecule was therefore advanced as a clinical candidate, and further details regarding its development will be reported in subsequent disclosures.

EXPERIMENTAL SECTION

Chemistry. All final compounds were purified to $\geq 95\%$ purity. For most compounds, purity was determined by Agilent 1200 or 1260 series HPLCs coupled to an Agilent 6120 or 6140 quadrupole LC/MS with simultaneous UV (220 and 254 nm) and TIC detection (either APCI or ESI) or using a Shimadzu LC-20 HPLC with UV 220 nm detection. Purity of compounds **12a** and **12b** was determined using an Agilent 1260 Infinity Hybrid HPLC/SFC with an Aurora AS SFC control module, DAD, Leap PAL autosampler, and 6120 single quadrupole MS detection. Purity of compounds **24a** and **24b** was determined using a Bruker XWIN-NMR (400 MHz) spectrometer with supporting data from chiral SFC analysis using the Agilent 1260 Infinity Hybrid HPLC/SFC.

Cell Culture. Human B-cell non-Hodgkin lymphoma cell line Karpas-422 was obtained from Deutsche Sammlung von Mikroorganismen und Zellkulturen (DSMZ) in Germany, catalog no. ACC-32. Cells were cultured in RPMI 1640 plus 10–20% (v/v) FBS and 1% Pen/Strep.

H3K27me3 ELISA Assay. Karpas-422 cells were plated in complete cell culture medium (100 μ L/well) in a 96-well clear, V bottom polystyrene cell culture plate (Costar, catalog no. 3894) at a density of 2500 cells/well. Cells were then incubated for 2–3 h at 37 °C and 5% CO₂. Compound dilution plates were prepared in 96-well, clear U-bottom, polypropylene plates (Corning, catalog no. 3365) in 100% DMSO at 10 mM stock concentration in duplicate wells, using an 11-point serial dilution (1:3 dilutions). Compounds were further diluted in growth medium, and an amount of 25 μ L was added to each

well of the cell plates using a Beckman FX liquid handling system such that the highest compound concentration tested was 50 μ M final, with a 0.5% final DMSO concentration. Plates were then incubated for 72 h at 37 °C and 5% CO₂. At the end of the incubation period with compound, plates were centrifuged at 2000 rpm for 5 min at room temperature and medium was removed. Then, 100 μ L of acid extracted solution was added to each well. Plates were shaken for 50 min at 4 °C to lyse cells, and then 38 μ L of neutralization buffer was added. Plates were then frozen at –80 °C. The next day, plates were shaken at room temperature to thaw. Cell lysates (50 μ L/well) were then transferred to ELISA plates. Plates were covered and incubated for 2.5 h at room temperature, with constant slow speed shaking. After incubation, plates were washed seven times (300 μ L/well) with 1× wash buffer using a BioTek plate washer. Then 100 μ L of biotinylated trimethyl histone H3K27 detection antibody was added to each well and incubated for 2 h at room temperature with constant slow speed shaking. After incubation, plates were washed as described. An amount of 100 μ L of HRP-linked antibody was added to each well and incubated for 60 min at room temperature with constant slow speed shaking. After incubation, plates were washed as described. Finally, 100 μ L of TMB substrate reagent was added to each well and incubated for 5 min at room temperature in the dark with slow shaking and 100 μ L of stop solution was added to stop the reaction. Plates were read on the PerkinElmer Envision plate reader using the 96-well with OD reading mode. The IC₅₀ values were determined from 11-point dose–response curves and were calculated using a four-parameter fit with GraphPad Prism or in house modified IDBS ActivityBase data analyzing package.

Cell Growth Inhibition Assay. Karpas-422 cells were plated in complete cell culture medium (100 μ L/well) in a 96-well clear, flat bottom polystyrene cell culture plate (Greiner, catalog no. 655182) at a density of 2000 cells/well. Cells were then incubated for 2–3 h at 37 °C and 5% CO₂. Compound dilution plates were prepared, and compounds were further diluted in growth medium as described above. Then, 25 μ L of the diluted compound was added to each well of the cell plates using a Beckman FX liquid handling system. Plates were then incubated for 72 h at 37 °C and 5% CO₂. At the end of the incubation period with compound, compounds were again diluted in growth medium and an amount of 30 μ L was added to each well of the cell plates using a Beckman FX liquid handling system. Plates were then incubated for 96 h at 37 °C and 5% CO₂. At the end of the incubation period, plates were centrifuged at 2000 rpm for 5 min at room temperature and medium was removed. Then 100 μ L of fresh complete cell culture medium was added to each well. Compounds were once more diluted in growth medium, and an amount of 25 μ L was added to each well of the cell plates using a Beckman FX liquid handling system. Plates were then incubated for 72 h at 37 °C and 5% CO₂. After the incubation period, plates were centrifuged at 2000 rpm for 5 min at room temperature and medium was removed. Then 100 μ L of fresh complete cell culture medium was added to each well. Finally, rezasurin in PBS (1 mg/mL) was added to each well of the cell plate (15 μ L/well). The plates were incubated at 37 °C and 5% CO₂ for 6 h in the dark. Plates were read on the PerkinElmer Envision plate reader using the 96-well with fluorescent reading mode at 530 nm excitation and 590 nm emissions. The IC₅₀ values were determined from 11-point dose–response curves and were calculated using a four-parameter fit with GraphPad Prism or in house modified IDBS ActivityBase data analyzing package.

Microsomal Stability Assay. Compounds (1 μ M) were incubated at 37 °C for 45 min in a final volume of 200 μ L of 100 mM potassium phosphate buffer (pH 7.4) containing pooled liver microsomes (0.8 mg/mL protein) and 2 mM NADPH. Reactions were initiated with the addition of NADPH following a 10 min preincubation. Aliquots of incubation samples were protein precipitated with cold methanol containing 0.1 μ M buspirone (internal standard) and centrifuged, and supernatants were analyzed by LC–MS/MS. All incubations were performed in triplicate. *In vitro* intrinsic clearance (CL_{int}) was calculated from half-life ($t_{1/2}$) of the parent drug disappearance, which was determined by the slope (k) of log–linear regression

analysis from the concentration versus time profiles, i.e., $t_{1/2} = -\ln(2)/k$.

Cell Culture and High Throughput Permeability Assay. The cell culturing conditions for in-house low efflux transporter MDCK (MDCK-LE) cell line (clonal cells isolated from Madin–Darby canine kidney cells, selected for low endogenous efflux transporter expression) were used to determine passive permeability. MDCK-LE cells were cultured at 37 °C, 5% CO₂, 95% relative humidity in minimum essential medium that contained 10% FBS, 1% NEAA, 100 U/mL penicillin, 100 µg/mL streptomycin, and 1% L-glutamine. Cells were passaged each week at about 90% confluence. Cells were trypsinized and resuspended in complete media to obtain a cell suspension of 2.5 × 10⁵ cells/mL and then plated onto 96-well membrane inserts, with each insert receiving a volume of 75 µL. The inserts were placed into a feeder tray containing complete growth medium. Plates were used on day 4 for transport studies. Cell inserts were washed with prewarmed transport buffer before the experiment. Monodirectional transport studies were performed with 2 µM drug solution in transport buffer with 0.1% DMSO. Drug solution was added to the donor wells, and buffer was added to the receiver wells to initiate the transport assay. The plates were incubated at 37 °C, and samples from both the donor and receiver were taken at time 0 and 90 min for LC–MS/MS analysis. Permeability was determined at donor pH 6.5 and 7.4, with receiver medium always at pH 7.4.

In Vivo Studies. All procedures performed on these animals were in accordance with regulations and established guidelines and were reviewed and approved by Pfizer's Institutional Animal Care and Use Committee.

■ ASSOCIATED CONTENT

Supporting Information

The Supporting Information is available free of charge on the ACS Publications website at DOI: [10.1021/acs.jmedchem.7b01375](https://doi.org/10.1021/acs.jmedchem.7b01375).

Synthetic experimental procedures, analytical data, and small molecule X-ray crystal structures for all compounds from Tables 1 and 2, enzymatic assay, biology experimental details, and computational method (PDF) Molecular formula strings and compound purity data (XLSX)

Accession Codes

PDB codes are the following: 6B3W for compound 1 complexed with EZH2/EED/SUZ12; 4W2R for compound 23a complexed with EZH2/EED/SUZ12.

■ AUTHOR INFORMATION

Corresponding Author

*E-mail: peipei.kung@pfizer.com. Phone: (858) 526-4867.

ORCID

Pei-Pei Kung: [0000-0002-9203-7374](https://orcid.org/0000-0002-9203-7374)

Notes

The authors declare no competing financial interest.

■ ACKNOWLEDGMENTS

We are grateful to Klaus Dress for data management and visualization help and to Jeff Elleraas, Loanne Chung, and Phuong Tran for purification assistance. We also thank Curtis Moore and Alex Yanovsky for small molecule X-ray structure determination.

■ ABBREVIATIONS USED

SMARCA2, SWI/SNF related, matrix associated, actin dependent regulator of chromatin, subfamily a, member 2; SMARCA4, SWI/SNF related, matrix associated, actin dependent regulator

of chromatin, subfamily a, member 4; ARID1A, AT-rich interaction domain 1A; SMARCB1, SWI/SNF related, matrix associated, actin dependent regulator of chromatin, subfamily b, member 1; SWI/SNF, switch/sucrose nonfermentable; log D, octanol-buffer (pH 7.4) distribution coefficient; MDCK-LE, Madin–Darby canine kidney, low efflux; CMC, carboxymethyl-cellulose; CEREP, Eurofins Cerep SA; MM-GBSA, molecular mechanics generalized born surface area

■ REFERENCES

- (1) Schuettengruber, B.; Cavalli, G. Recruitment of polycomb group complexes and their role in the dynamic regulation of cell fate choice. *Development* **2009**, *136*, 3531–3542.
- (2) Lewis, E. B. A gene complex controlling segmentation in *Drosophila*. *Nature* **1978**, *276*, 565–570.
- (3) Margueron, R.; Reinberg, D. The polycomb complex PRC2 and its mark in life. *Nature* **2011**, *469*, 343–349.
- (4) Di Croce, L.; Helin, K. Transcriptional regulation by polycomb group proteins. *Nat. Struct. Mol. Biol.* **2013**, *20*, 1147–1155.
- (5) Yamaguchi, H.; Hung, M. C. Regulation and role of EZH2 in cancer. *Cancer Res. Treat.* **2014**, *46*, 209–222.
- (6) Morin, R. D.; Johnson, N. A.; Severson, T. M.; Mungall, A. J.; An, J.; Goya, R.; Paul, J. E.; Boyle, M.; Woolcock, B. W.; Kuchenbauer, F.; Yap, D.; Humphries, R. K.; Griffith, O. L.; Shah, S.; Zhu, H.; Kimbara, M.; Shashkin, P.; Charlot, J. F.; Tcherpakov, M.; Corbett, R.; Tam, A.; Varhol, R.; Smailus, D.; Moksa, M.; Zhao, Y.; Delaney, A.; Qian, H.; Birol, I.; Schein, J.; Moore, R.; Holt, R.; Horsman, D. E.; Connors, J. M.; Jones, S.; Aparicio, S.; Hirst, M.; Gascoyne, R. D.; Marra, M. A. Somatic mutations altering EZH2 (Tyr641) in follicular and diffuse large B-cell lymphomas of germinal-center origin. *Nat. Genet.* **2010**, *42*, 181–185.
- (7) Morin, R. D.; Mendez-Lago, M.; Mungall, A. J.; Goya, R.; Mungall, K. L.; Corbett, R. D.; Johnson, N. A.; Severson, T. M.; Chiu, R.; Field, M.; Jackman, S.; Krzywinski, M.; Scott, D. W.; Trinh, D. L.; Tamura-Wells, J.; Li, S.; Firme, M. R.; Rogic, S.; Griffith, M.; Chan, S.; Yakovenko, O.; Meyer, I. M.; Zhao, E. Y.; Smailus, D.; Moksa, M.; Chittaranjan, S.; Rimsza, L.; Brooks-Wilson, A.; Spinelli, J. J.; Ben-Neriah, S.; Meissner, B.; Woolcock, B.; Boyle, M.; McDonald, H.; Tam, A.; Zhao, Y.; Delaney, A.; Zeng, T.; Tse, K.; Butterfield, Y.; Birol, I.; Holt, R.; Schein, J.; Horsman, D. E.; Moore, R.; Jones, S. J.; Connors, J. M.; Hirst, M.; Gascoyne, R. D.; Marra, M. A. Frequent mutation of histone-modifying genes in non-Hodgkin lymphoma. *Nature* **2011**, *476*, 298–303.
- (8) McCabe, M. T.; Graves, A. P.; Ganji, G.; Diaz, E.; Halsey, W. S.; Jiang, Y.; Smitheman, K. N.; Ott, H. M.; Pappalardi, M. B.; Allen, K. E.; Chen, S. B.; Della Pietra, A., 3rd; Dul, E.; Hughes, A. M.; Gilbert, S. A.; Thrall, S. H.; Tummino, P. J.; Kruger, R. G.; Brandt, M.; Schwartz, B.; Creasy, C. L. Mutation of A677 in histone methyltransferase EZH2 in human B-cell lymphoma promotes hypertrimethylation of histone H3 on lysine 27 (H3K27). *Proc. Natl. Acad. Sci. U. S. A.* **2012**, *109*, 2989–2994.
- (9) Sneeringer, C. J.; Scott, M. P.; Kuntz, K. W.; Knutson, S. K.; Pollock, R. M.; Richon, V. M.; Copeland, R. A. Coordinated activities of wild-type plus mutant EZH2 drive tumor-associated hypertrimethylation of lysine 27 on histone H3 (H3K27) in human B-cell lymphomas. *Proc. Natl. Acad. Sci. U. S. A.* **2010**, *107*, 20980–20985.
- (10) McCabe, M. T.; Ott, H. M.; Ganji, G.; Korenchuk, S.; Thompson, C.; Van Aller, G. S.; Liu, Y.; Graves, A. P.; Della Pietra, A., III; Diaz, E.; LaFrance, L. V.; Mellinger, M.; Duquenne, C.; Tian, X.; Kruger, R. G.; McHugh, C. F.; Brandt, M.; Miller, W. H.; Dhanak, D.; Verma, S. K.; Tummino, P. J.; Creasy, C. L. EZH2 inhibition as a therapeutic strategy for lymphoma with EZH2-activating mutations. *Nature* **2012**, *492*, 108–112.
- (11) Wang, Y.; Chen, S. Y.; Karnezis, A. N.; Colborne, S.; Santos, N. D.; Lang, J. D.; Hendricks, W. P.; Orlando, K. A.; Yap, D.; Komoss, F.; Bally, M. B.; Morin, G. B.; Trent, J. M.; Weissman, B. E.; Huntsman, D. G. The histone methyltransferase EZH2 is a therapeutic

- target in small cell carcinoma of the ovary, hypercalcaemic type. *J. Pathol.* **2017**, *242*, 371–383.
- (12) Chan-Penebre, E.; Armstrong, K.; Drew, A.; Grassian, A. R.; Feldman, I.; Knutson, S. K.; Kuplast-Barr, K.; Roche, M.; Campbell, J.; Ho, P.; Copeland, R. A.; Chesworth, R.; Smith, J. J.; Keilhack, H.; Ribich, S. A. Selective killing of SMARCA2- and SMARCA4-deficient small cell carcinoma of the ovary, hypercalcemic type cells by inhibition of EZH2: *in vitro* and *in vivo* preclinical models. *Mol. Cancer Ther.* **2017**, *16*, 850–860.
- (13) Bitler, B. G.; Aird, K. M.; Garipov, A.; Li, H.; Amatangelo, M.; Koskenkov, A. V.; Schultz, D. C.; Liu, Q.; Shih, I.-M.; Conejo-Garcia, J. R.; Speicher, D. W.; Zhang, R. Synthetic lethality by targeting EZH2 methyltransferase activity in ARID1A-mutated cancers. *Nat. Med.* **2015**, *21*, 231–238.
- (14) Wilson, B. G.; Roberts, C. W. SWI/SNF nucleosome remodelers and cancer. *Nat. Rev. Cancer* **2011**, *11*, 481–492.
- (15) Kim, K. H.; Kim, W.; Howard, T. P.; Vazquez, F.; Tsherniak, A.; Wu, J. N.; Wang, W.; Haswell, J. R.; Walensky, L. D.; Hahn, W. C.; Orkin, S. H.; Roberts, C. W. SWI/SNF-mutant cancers depend on catalytic and non-catalytic activity of EZH2. *Nat. Med.* **2015**, *21*, 1491–1496.
- (16) Kawano, S.; Grassian, A. R.; Tsuda, M.; Knutson, S. K.; Warholic, N. M.; Kuznetsov, G.; Xu, S.; Xiao, Y.; Pollock, R. M.; Smith, J. S.; Kuntz, K. K.; Ribich, S.; Minoshima, Y.; Matsui, J.; Copeland, R. A.; Tanaka, S.; Keilhack, H. Preclinical evidence of anti-tumor activity induced by EZH2 inhibition in human models of synovial sarcoma. *PLoS One* **2016**, *11*, e0158888 DOI: 10.1371/journal.pone.0158888.
- (17) Gardner, E. E.; Lok, B. H.; Schneeberger, V. E.; Desmeules, P.; Miles, L. A.; Arnold, P. K.; Ni, A.; Khodos, I.; de Stanchina, E.; Nguyen, T.; Sage, J.; Campbell, J. E.; Ribich, S.; Rekhtman, N.; Dowlati, A.; Massion, P. P.; Rudin, C. M.; Poirier, J. T. Chemosensitive relapse in small cell lung cancer proceeds through an EZH2-SLFN11 axis. *Cancer Cell* **2017**, *31*, 286–299.
- (18) Dardenne, E.; Beltran, H.; Benelli, M.; Gayvert, K.; Berger, A.; Puca, L.; Cyrt, J.; Sboner, A.; Noorizad, Z.; MacDonald, T.; Cheung, C.; Yuen, K. S.; Gao, D.; Chen, Y.; Eilers, M.; Mosquera, J. M.; Robinson, B. D.; Elemento, O.; Rubin, M. A.; Demichelis, F.; Rickman, D. S. N-myc induces an EZH2-mediated transcriptional program driving neuroendocrine prostate cancer. *Cancer Cell* **2016**, *30*, 563–577.
- (19) Ku, S. Y.; Rosario, S.; Wang, Y.; Mu, P.; Seshadri, M.; Goodrich, Z. W.; Goodrich, M. M.; Labbe, D. P.; Gomez, E. C.; Wang, J.; Long, H. W.; Xu, B.; Brown, M.; Loda, M.; Sawyers, C. L.; Ellis, L.; Goodrich, D. W. Rb1 and Trp53 cooperate to suppress prostate cancer lineage plasticity, metastasis, and antiandrogen resistance. *Science* **2017**, *355*, 78–83.
- (20) Knutson, S. K.; Kawano, S.; Minoshima, Y.; Warholic, N. M.; Huang, K. C.; Xiao, Y.; Kadowaki, T.; Uesugi, M.; Kuznetsov, G.; Kumar, N.; Wigle, T. J.; Klaus, C. R.; Allain, C. J.; Raimondi, A.; Waters, N. J.; Smith, J. J.; Porter-Scott, M.; Chesworth, R.; Moyer, M. P.; Copeland, R. A.; Richon, V. M.; Uenaka, T.; Pollock, R. M.; Kuntz, K. W.; Yokoi, A.; Keilhack, H. Selective inhibition of EZH2 by EPZ-6438 leads to potent antitumor activity in EZH2-mutant non-Hodgkin lymphoma. *Mol. Cancer Ther.* **2014**, *13*, 842–854.
- (21) Vaswani, R. G.; Gehling, V. S.; Dakin, L. A.; Cook, A. S.; Nasveschuk, C. G.; Duplessis, M.; Iyer, P.; Balasubramanian, S.; Zhao, F.; Good, A. C.; Campbell, R.; Lee, C.; Cantone, N.; Cummings, R. T.; Normant, E.; Bellon, S. F.; Albrecht, B. K.; Harmange, J. C.; Trojer, P.; Audia, J. E.; Zhang, Y.; Justin, N.; Chen, S.; Wilson, J. R.; Gamblin, S. J. Identification of (R)-N-((4-methoxy-6-methyl-2-oxo-1,2-dihydropyridin-3-yl)methyl)-2-methyl-1-(1-(1-(2,2,2-trifluoroethyl)piperidin-4-yl)ethyl)-1H-indole-3-carboxamide (CPI-1205), a potent and selective inhibitor of histone methyltransferase EZH2, suitable for phase I clinical trials for B-cell lymphomas. *J. Med. Chem.* **2016**, *59*, 9928–9941.
- (22) Morschhauser, F.; Salles, G.; McKay, P.; Tilly, H.; Schmitt, A.; Gerecitano, J.; Johnson, P.; Le Gouill, S.; Dickinson, M. J.; Fruchart, C.; Lamy, T.; Chaidos, A.; Jurczak, W.; Opat, S.; Radford, J.; Zinzani, P. L.; Assouline, S.; Cartron, G.; Clawson, A.; Picazio, N.; Ribich, S.; Blakemore, S. J.; Larus, J.; Miao, H.; Woodruff, M.; Ho, P. T.; Ribrag, V. Interim report from a phase II multicenter study of tazemetostat, an EZH2 inhibitor: clinical activity and favorable safety in patients with relapsed or refractory B-cell non-Hodgkin lymphoma. Presented at the 14th International Conference on Malignant Lymphoma, Switzerland, June 14–17, 2017.
- (23) (a) Qi, W.; Zhao, K.; Gu, J.; Huang, Y.; Wang, Y.; Zhang, H.; Zhang, M.; Zhang, J.; Yu, Z.; Li, L.; Teng, L.; Chuai, S.; Zhang, C.; Zhao, M.; Chan, H.; Chen, Z.; Fang, D.; Fei, Q.; Feng, L.; Feng, L.; Gao, Y.; Ge, H.; Ge, X.; Li, G.; Lingel, A.; Lin, Y.; Liu, Y.; Luo, F.; Shi, M.; Wang, L.; Wang, Z.; Yu, Y.; Zeng, J.; Zeng, C.; Zhang, L.; Zhang, Q.; Zhou, S.; Oyang, C.; Atadja, P.; Li, E. An allosteric PRC2 inhibitor targeting the H3K27me3 binding pocket of EED. *Nat. Chem. Biol.* **2017**, *13*, 381–388. (b) He, Y.; Selvaraju, S.; Curtin, M. L.; Jakob, C. G.; Zhu, H.; Comess, K. M.; Shaw, B.; The, J.; Lima-Fernandes, E.; Szewczyk, M. M.; Cheng, D.; Klinge, K. L.; Li, H. Q.; Pliushchev, M.; Algire, M. A.; Maag, D.; Guo, J.; Dietrich, J.; Panchal, S. C.; Petros, A. M.; Sweis, R. F.; Torrent, M.; Bigelow, L. J.; Semisterra, G.; Li, F.; Kennedy, S.; Wu, Q.; Osterling, D. J.; Lindley, D. J.; Gao, W.; Galasinski, S.; Barsyte-Lovejoy, D.; Vedadi, M.; Buchanan, F. G.; Arrowsmith, C. H.; Chiang, G. G.; Sun, C.; Pappano, W. N. The EED protein-protein interaction inhibitor A-395 inactivates the PRC2 complex. *Nat. Chem. Biol.* **2017**, *13*, 389–395.
- (24) Kung, P. P.; Rui, E.; Bergqvist, S.; Bingham, P.; Braganza, J.; Collins, M.; Cui, M.; Diehl, W.; Dinh, D.; Fan, C.; Fantin, V. R.; Gukasyan, H. J.; Hu, W.; Huang, B.; Kephart, S.; Krivacic, C.; Kumpf, R. A.; Li, G.; Maegley, K. A.; McAlpine, I.; Nguyen, L.; Ninkovic, S.; Ornelas, M.; Ryskin, M.; Scales, S.; Sutton, S.; Tatlock, J.; Verhelle, D.; Wang, F.; Wells, P.; Wythes, M.; Yamazaki, S.; Yip, B.; Yu, X.; Zehnder, L.; Zhang, W. G.; Rollins, R. A.; Edwards, M. Design and synthesis of pyridone-containing 3,4-dihydroisoquinoline-1(2H)-ones as a novel class of enhancer of zeste homolog 2 (EZH2) inhibitors. *J. Med. Chem.* **2016**, *59*, 8306–8325.
- (25) (a) Hosea, N. A.; Collard, W. T.; Cole, S.; Maurer, T. S.; Fang, R. X.; Jones, H.; Kakar, S. M.; Nakai, Y.; Smith, B. J.; Webster, R.; Beaumont, K. Prediction of human pharmacokinetics from preclinical information: comparative accuracy of quantitative prediction approaches. *J. Clin. Pharmacol.* **2009**, *49*, 513–533. (b) Human microsomal $Cl_{int,app}$ ($\mu\text{L}/\text{min}/\text{mg}$ protein) bins: <9 (low), 9–49 (moderate), and >49 (high).
- (26) Varma, M. V.; Gardner, I.; Steyn, S. J.; Nkansah, P.; Rotter, C. J.; Whitney-Pickett, C.; Zhang, H.; Di, L.; Cram, M.; Fenner, K. S.; El-Kattan, A. F. pH-Dependent solubility and permeability criteria for provisional biopharmaceutics classification (BCS and BDDCS) in early drug discovery. *Mol. Pharmaceutics* **2012**, *9*, 1199–1212.
- (27) Hill, A. P.; Young, R. J. Getting physical in drug discovery: a contemporary perspective on solubility and hydrophobicity. *Drug Discovery Today* **2010**, *15*, 648–655.
- (28) Lovering, F.; Bikker, J.; Humblet, C. Escape from flatland: increasing saturation as an approach to improving clinical success. *J. Med. Chem.* **2009**, *52*, 6752–6756.
- (29) Yap, D. B.; Chu, J.; Berg, T.; Schapira, M.; Cheng, S. W.; Moradian, A.; Morin, R. D.; Mungall, A. J.; Meissner, B.; Boyle, M.; Marquez, V. E.; Marra, M. A.; Gascoyne, R. D.; Humphries, R. K.; Arrowsmith, C. H.; Morin, G. B.; Aparicio, S. A. Somatic mutations at EZH2 Y641 act dominantly through a mechanism of selectively altered PRC2 catalytic activity, to increase H3K27 trimethylation. *Blood* **2011**, *117*, 2451–2459.
- (30) Ryckmans, T.; Edwards, M. P.; Horne, V. A.; Correia, A. M.; Owen, D. R.; Thompson, L. R.; Tran, I.; Tutt, M. F.; Young, T. Rapid assessment of a novel series of selective CB(2) agonists using parallel synthesis protocols: A lipophilic efficiency (LipE) analysis. *Bioorg. Med. Chem. Lett.* **2009**, *19*, 4406–4409.
- (31) Stepan, A. F.; Kauffman, G. W.; Keefer, C. E.; Verhoest, P. R.; Edwards, M. Evaluating the differences in cycloalkyl ether metabolism using the design parameter “lipophilic metabolism efficiency” (LipMetE) and a matched molecular pairs analysis. *J. Med. Chem.* **2013**, *56*, 6985–6990.

(32) Brooun, A.; Gajiwala, K. S.; Deng, Y. L.; Liu, W.; Bolanos, B.; Bingham, P.; He, Y. A.; Diehl, W.; Grable, N.; Kung, P. P.; Sutton, S.; Maegley, K. A.; Yu, X.; Stewart, A. E. Polycomb repressive complex 2 structure with inhibitor reveals a mechanism of activation and drug resistance. *Nat. Commun.* **2016**, *7*, 11384.

(33) The coordinate error for a 3 Å crystal structure is between 0.2 and 0.3 Å. Therefore, we believe that the two compounds make hydrogen bonds of similar strength to the key residues (Trp624 and Tyr111).

(34) (a) Jiao, L.; Liu, X. Structural basis of histone H3K27 trimethylation by an active polycomb repressive complex 2. *Science* **2015**, *350*, aac4383. (b) Justin, N.; Zhang, Y.; Tarricone, C.; Martin, S. R.; Chen, S.; Underwood, E.; De Marco, V.; Haire, L. F.; Walker, P. A.; Reinberg, D.; Wilson, J. R.; Gamblin, S. J. Structural basis of oncogenic histone H3K27M inhibition of human polycomb repressive complex 2. *Nat. Commun.* **2016**, *7*, 11316.

(35) Tsuzuki, S.; Honda, K.; Uchimaru, T.; Mikami, M.; Fujii, A. Magnitude and directionality of the interaction energy of the aliphatic CH/π interaction: significant difference from hydrogen bond. *J. Phys. Chem. A* **2006**, *110*, 10163–10168.

(36) Hoffmann, R. W. Allylic 1,3-strain as a controlling factor in stereoselective transformations. *Chem. Rev.* **1989**, *89*, 1841–1860.

(37) Taylor, R.; Kennard, O. Hydrogen-bond geometry in organic crystals. *Acc. Chem. Res.* **1984**, *17*, 320–326.

(38) Li, A.; Ouyang, Y.; Wang, Z.; Cao, Y.; Liu, X.; Ran, L.; Li, C.; Li, L.; Zhang, L.; Qiao, K.; Xu, W.; Huang, Y.; Zhang, Z.; Tian, C.; Liu, Z.; Jiang, S.; Shao, Y.; Du, Y.; Ma, L.; Wang, X.; Liu, J. Novel pyridinone derivatives as non-nucleoside reverse transcriptase inhibitors (NNRTIs) with high potency against NNRTI-resistant HIV-1 strains. *J. Med. Chem.* **2013**, *56*, 3593–3608.

(39) Lin, C. H.; Tsai, M. R.; Wang, Y. S.; Chang, N. C. An efficient approach to 3,4-disubstituted pyridin-2-ones. formal synthesis of mappicine ketone. *J. Org. Chem.* **2003**, *68*, 5688–5691.

(40) Hama, T.; Liu, X.; Culkin, D. A.; Hartwig, J. F. Palladium-catalyzed α-arylation of esters and amides under more neutral conditions. *J. Am. Chem. Soc.* **2003**, *125*, 11176–11177.

(41) Li-Yuan Bao, R.; Zhao, R.; Shi, L. Progress and developments in the turbo Grignard reagent i-PrMgCl·LiCl: a ten-year journey. *Chem. Commun.* **2015**, *51*, 6884–6900.

(42) For an alternative synthesis of oxetane-3-carbaldehyde see the following: Kephart, S. E.; Zehnder, L. R.; Huang, B.; Sutton, S. C. Synthesis of oxetane-3-carboxaldehyde and methyl oxetane-3-carboxylate via homologation of oxetane-3-one. *Tetrahedron* **2016**, *72*, 3641–3646.

(43) Wang, Z.; Chen, Z.; Sun, J. Catalytic asymmetric nucleophilic openings of 3-substituted oxetanes. *Org. Biomol. Chem.* **2014**, *12*, 6028–6032.